



Role of the upper ocean in the energy budget of Arctic sea ice during SHEBA

W. J. Shaw,¹ T. P. Stanton,¹ M. G. McPhee,² J. H. Morison,³ and D. G. Martinson^{4,5}

Received 15 July 2008; revised 24 February 2009; accepted 17 March 2009; published 12 June 2009.

[1] As part of the 1997–1998 Surface Heat Budget of the Arctic Experiment (SHEBA), a nearly yearlong record of upper ocean observations was obtained below a drifting ice camp in the Beaufort Gyre. A combination of observational and numerical modeling techniques are used to estimate heat fluxes across the under-ice ocean boundary layer. Over the Canada Basin, the upper pycnocline contained moderate heat, but strong stratification effectively insulated it from mixed layer turbulence. Average resulting heat fluxes at the base of the mixed layer (F_{pyc}) and at the ocean-ice interface (F_0) were small (0.3 – 1.2 and 0.2 W m^{-2} , respectively). Over the Chukchi Borderlands, the presence of relatively warm and salty Pacific origin water increased upper pycnocline heat content and reduced stratification, which permitted moderate F_{pyc} and F_0 (2.1 – 3.7 and 3.5 W m^{-2} , respectively). Solar insolation was the dominant heat source during the final, summertime portion of the drift. During the heating period, F_{pyc} was relatively small (0.4 – 1.5 W m^{-2}) while F_0 was large (16.3 W m^{-2}). The drift-averaged value of F_0 was 7.6 W m^{-2} . Energy budgets for the ice cover were constructed. The oceanic contribution to the budget during the portion of the drift over the Chukchi Borderlands, supported by entrainment of heat stored in the upper pycnocline, was responsible for a 15% reduction in ice growth. During the summer heating season, the F_0 estimates were larger than the latent energy changes associated with basal melting.

Citation: Shaw, W. J., T. P. Stanton, M. G. McPhee, J. H. Morison, and D. G. Martinson (2009), Role of the upper ocean in the energy budget of Arctic sea ice during SHEBA, *J. Geophys. Res.*, 114, C06012, doi:10.1029/2008JC004991.

1. Introduction

[2] The Arctic Ocean plays an important role in global climate change because of its sensitivity to positive feedbacks such as the ice-albedo feedback mechanism [Kellog, 1973; Curry *et al.*, 1995]. These feedbacks are governed by energy exchange processes between the ice, the overlying atmospheric boundary layer, and the underlying oceanic boundary layer that in turn govern the mass balance of sea ice. Meaningful predictions of ice thickness and concentration, therefore, require an understanding of surface energy fluxes in both the atmosphere and the ocean. This paper focuses on the role of the oceanic heat flux in the energy budget of sea ice as observed in the western Arctic during the 1997–1998 Surface Heat Budget of the Arctic (SHEBA) experiment.

1.1. Ocean-to-Ice Heat Flux

[3] Ocean-to-ice heat flux F_0 is controlled by the magnitude of turbulent transfer rates in the under-ice ocean boundary layer (IOBL), the heat content of the IOBL and the upper pycnocline, and the strength of stratification of the upper pycnocline. Variability in F_0 is expected to arise from spatial and temporal changes in stratification and heat content. Arctic upper ocean stratification varies seasonally because of melt and growth of sea ice and geographically because of proximity to river inputs. Heat sources in the upper Arctic Ocean include local radiative heating through thin ice and leads, advection of Atlantic and Pacific origin waters, and near-surface advection of radiatively heated water from ice-free areas within the Arctic. Resultant heat content varies seasonally because of the annual cycle in radiative forcing and it varies geographically because of proximity to open water and the pathways followed by Atlantic and Pacific Water.

[4] Previous research finds that local radiative heating of the IOBL through thin ice and leads during summer is the dominant source of heat supporting F_0 . Early theoretical work using sea ice thermodynamic models established that a 2 W m^{-2} ocean-to-ice heat flux was required to maintain observed perennial sea ice thickness [Maykut and Untersteiner, 1971]. Using ice strain data from the 1975 Arctic Ice Dynamics Joint Experiment (AIDJEX) in the Beaufort Sea and climatological radiation values, Maykut [1982] estimated that an average of 3.2 W m^{-2} of shortwave energy is absorbed

¹Oceanography Department, Naval Postgraduate School, Monterey, California, USA.

²McPhee Research Company, Naches, Washington, USA.

³Polar Science Center, Applied Physics Laboratory, University of Washington, Seattle, Washington, USA.

⁴Lamont-Doherty Earth Observatory, Earth Institute at Columbia University, Palisades, New York, USA.

⁵Department of Earth and Environmental Sciences, Columbia University, Palisades, New York, USA.

in the upper ocean, enough to provide the canonical ocean-to-ice heat flux of *Maykut and Untersteiner* [1971]. Further work based on AIDJEX observations refined these results. Using “bulk” estimates of F_0 and estimates of shortwave radiation penetrating into the upper ocean from measured radiation and ice concentration inferred from measured deformation, *Maykut and McPhee* [1995] find that radiative energy fluxes entering the IOBL are large enough to support an estimated annual average F_0 of 5.1 W m^{-2} in the central Arctic, without need for additional heat sources.

[5] A second potential heat source to support F_0 is vertical turbulent transport to the IOBL from heat-carrying Atlantic or Pacific origin layers within the halocline. Large-scale advection of heat in the Arctic is dominated by the circulation at depth of relatively warm Atlantic Layer water. Throughout most of the Arctic though, Atlantic Layer water is thermodynamically decoupled from the IOBL by the strong salinity stratification of the cold halocline [*Aagaard et al.*, 1981]. This is why in the central Arctic, at least, there is a rough balance between radiation entering the upper ocean and F_0 when integrated over seasonal time scales [*Maykut and McPhee*, 1995].

[6] In some areas of the Arctic though, there is suggestion and some direct evidence that F_0 is supported by entrainment of heat transported in layers below the IOBL. For example, F_0 estimates obtained as a pair of autonomous buoys drifted over the Yermak plateau show that large surface heat fluxes (22 W m^{-2}) were supported by entrainment of relatively warm Atlantic Layer water [*McPhee et al.*, 2003]. In this case, the large entrainment heat fluxes were likely due to elevated turbulence levels in the halocline associated with internal waves interacting with the local topography [*D’Asaro and Morison*, 1992] and the lack of a fully developed cold halocline in this “upstream” area. In another example of Atlantic Layer influence, *Walsh et al.* [2007] describe the potential significance of vertical heat fluxes from the Atlantic Layer in the eastern Nansen Basin.

[7] Smaller, but still significant [*Woodgate et al.*, 2005], amounts of heat are transported into the Arctic from the Pacific through the shallow Bering Straits, and Pacific origin water may serve as an additional advective heat source. Pacific Water, with modifications over the Chukchi Shelf, occupies the upper pycnocline of portions of the western Arctic and this layer often contains a shallow, subsurface temperature maximum [*Shimada et al.*, 2001], although the relative contributions of insolation over the shelf and direct advection from the Bering Sea to the heat content of this layer is uncertain. In contrast to the Atlantic Layer, heat-containing Pacific Water is not thermodynamically decoupled from the IOBL; and it has been suggested that this heat source may play a role in the regional ice mass balance [*Shimada et al.*, 2001; *Steele et al.*, 2004]. For example, *Shimada et al.* [2001] suggest that the presence of unusually warm Pacific origin water over the Northwind Ridge and Chukchi Plateau in the winter of 1997–1998 preconditioned the water column to promote a large reduction in ice concentration in the that area in summer 1998. Observations of systematic changes in the Arctic Ocean, including shifts in the position of the front that separates halocline waters of Pacific and Atlantic origin [*Morison et al.*, 2006, 2007] and a retreat [*Steele and Boyd*, 1998] and

partial recovery [*Gunn and Muench*, 2001; *Boyd et al.*, 2002] of the extent of the cold halocline, have rekindled interest in the significance of vertical transport to the IOBL of heat transported from the Atlantic and Pacific.

1.2. SHEBA Experiment

[8] SHEBA was executed to quantify and understand heat exchange through the high-latitude, atmosphere-ice-ocean system (see *Uttal et al.* [2002] for experiment overview and *Perovich and Moritz* [2002] for preface to *Journal of Geophysical Research—Oceans* SHEBA special section). The nearly yearlong SHEBA field program was run from a camp established on a multiyear ice floe in the western Arctic (Figure 1) supported by a Canadian Coast Guard icebreaker *Des Groseillers*. The resulting observations have afforded a unique view of air-sea-ice interaction processes in the Arctic: simultaneous measurements in the atmospheric boundary layer, the ice, and the ocean surface boundary layer over a complete annual cycle. There are a number of publications based on the SHEBA observations that address upper ocean conditions and the surface heat budget of the Arctic on which this study seeks to build.

[9] The SHEBA ice group made direct measurements of ice thickness and temperature at multiple sites, documenting the ice mass balance [*Perovich et al.*, 2003] and indirectly estimating F_0 as the residual of an ice base energy balance [*Perovich and Elder*, 2002] (see also section 5). *Perovich et al.* [2003] observed that ice thickness at the SHEBA field site was unexpectedly thin and that additional ice mass was lost over the observation period. Combining results from all of their sites, they found an average winter growth of 0.51 m and a summer melt of 1.26 m, which consisted of 0.64 m of surface melt and 0.62 m of bottom melt. *Perovich and Elder* [2002] find that annually averaged F_0 range from $7.5\text{--}12.4 \text{ W m}^{-2}$ depending on ice type.

[10] The SHEBA atmospheric boundary layer group has described the energy budget at the air-ice interface using estimates of all of the atmospheric energy flux terms at a single site [*Persson et al.*, 2002]. The annual average of the sum of all the atmospheric energy flux components provides a best estimate of the net surface flux excess of 8.2 W m^{-2} which is in close agreement to the 8.4 W m^{-2} implied by the observed surface melting at SHEBA [*Perovich et al.*, 2003].

[11] Most of the work based on SHEBA ocean measurements has focused on the origins of the unusually warm and fresh upper ocean seen at the beginning of the experiment [*McPhee et al.*, 1998; *Macdonald et al.*, 2002; *Kadko and Swart*, 2004], the distribution and spreading pathways of Pacific origin water [*Shimada et al.*, 2001; *McLaughlin et al.*, 2004], or the description of significant events observed during the field campaign [*McPhee et al.*, 2005; *Skyllingstad et al.*, 2005]. *McPhee et al.* [2005] describe a period of intense ocean heat flux and upwelling associated with concentrated ice deformation. *Skyllingstad et al.* [2005] describe the “mix-down” of surface-trapped meltwater that led to the development of the 1998 summer mixed layer. Additionally, *Hayes* [2003] and *Hayes and Morison* [2008] have discussed additional measurements of summer ocean-to-ice heat flux using an autonomous underwater vehicle and aspects of the summer surface mixed layer heat budget.

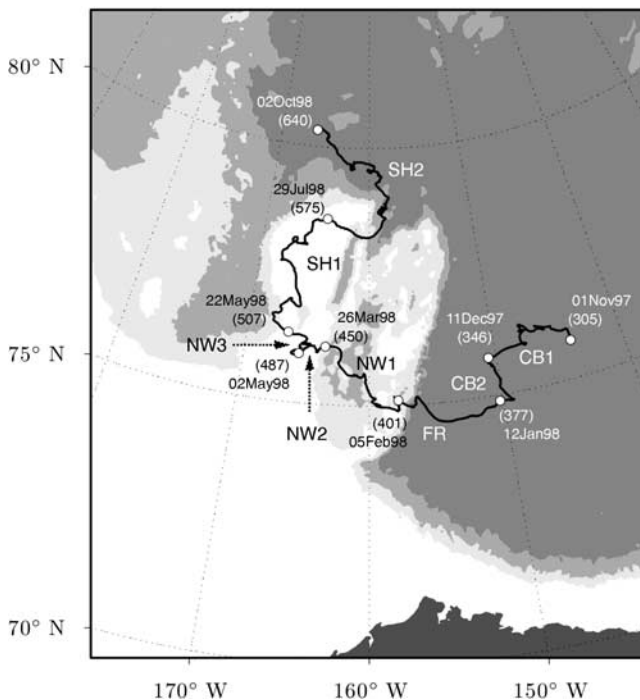


Figure 1. Bathymetric map of the western Arctic Ocean with drift track of the SHEBA ice camp. The white dots on the drift track, labeled with corresponding date and yearday, mark the positions of the boundaries between the drift segments discussed in the text, and the segments themselves are identified using the nomenclature developed in the text. Contour interval is 1000 m.

1.3. Objectives

[12] In this paper, we use the SHEBA ocean observations, supplemented with the output of a numerical IOBL model (the Steady Local Turbulence Closure (SLTC) model of *McPhee* [1999]), to investigate the contribution of the upper ocean to the ice cover energy balance. The specific objectives are to (1) describe the stability and heat content of the upper ocean; (2) quantify the variation and annual means of heat fluxes across the ocean boundary layer during the SHEBA observation period, including the entrainment of heat into the surface layer from the upper pycnocline; and (3) quantify the significance of F_0 in the ice cover energy budget. Our present study adds to the previous SHEBA results by providing best estimates of heat flux at the ocean-ice interface and at the base of the well-mixed surface layer. The ocean heat fluxes provide the link between the previous hydrographic work and the surface heat budget.

[13] Estimates of entrainment fluxes at the mixed layer base allow us to directly evaluate the significance to the ice cover energy budget of vertical heat transport from the upper pycnocline. We take advantage of the results of the SHEBA atmospheric boundary layer and ice groups to place the ocean measurements in context and assess the role of the ocean in the surface heat budget. The F_0 estimates are used to directly test an energy budget for the base of the ice cover, and we also construct and test an overall budget for the ice cover that includes the ocean and atmospheric fluxes and changes in internal energy of the ice cover.

[14] The remainder of this paper is organized as follows: descriptions of the SHEBA ocean observations (section 2) and the SLTC modeling effort (section 3), presentations of upper ocean conditions and heat fluxes (section 4) and ice cover energy heat budgets (section 5), followed by a discussion (section 6) and a summary and conclusions (section 7).

2. Ocean Observations

[15] The upper ocean observations presented here were obtained using three sensor suites deployed below the ice through hydroholes: an automated, profiling CTD, a fast response microstructure package designed to resolve the spatial scales of turbulent thermal variance dissipation, and a vertical array of turbulence sensors designed to measure flux-carrying turbulence scales. The observations are remarkable in that they resolve fine-scale vertical structure and temporal variability of the IOBL and pycnocline over an annual cycle. Data from the three systems are used to provide heat flux estimates at two vertical levels within the IOBL. The vertical array of flux sensors provides heat flux estimates within the IOBL. Thermal microstructure data are used to estimate heat fluxes at the base of the well-mixed surface layer. All of these heat flux estimates are subject to technical and/or theoretical limitations, which are detailed in the following sections. For example, as was expected for such an undertaking, there were occasional gaps in the data collection when sensors needed maintenance or the logistic infrastructure had to be adjusted to changing ice conditions. Another limitation of the observations is that during summer, when insolation complicates the vertical structure of the IOBL, it is difficult to extrapolate observational heat flux estimates to values at the ice-ocean interface. The observational heat flux estimates are thus supplemented with the SLTC numerical boundary layer model that is run with observed surface forcing and temperature and salinity structure (see section 3). Model output provides heat flux comparisons for the two observational levels as well as estimates of the interface fluxes. A common, 3-h time base is set up, over which the observations are ensemble averaged and for which an SLTC run is performed. The 3-h interval is a good compromise between achieving statistical stationarity with the turbulence estimates and resolving temporal variability of the “mean” characteristics of the IOBL.

2.1. Profiling CTD

[16] The high-resolution, profiling CTD was a pumped, dual-sensor Sea-Bird 911, run topside from an automated winch and data acquisition system. The microstructure package, composed of two fast response thermistors, was mounted at the bottom of the CTD cage. The profiler cycled via the computer-controlled winch between approximately 5 and 150 m depth at a nominal speed of 0.35 m s^{-1} for a 15 min return time. The CTD data were processed using the alignment, filtering, and thermal lag correction techniques recommended by Sea-Bird. Only data from the downgoing portions of the casts are utilized here, because the fast thermistor sensors were obstructed by the CTD on the upgoing portions.

[17] A total of 12,350 downcasts were obtained during the field program. There were 21 days for which no casts

were made; 9 occurred between days 447 and 455 when the development of a pressure ridge forced relocation of all the oceanographic instruments. Typically, the profiler ran for between 6 and 12 h a day; operating at this 25–50% duty cycle with a 15 min return time resulted in between 24 and 48 profiles per day. The number of casts per day increased to about 96 during the last two months of the experiment. In terms of the 3-h ensemble averaging periods, 60% had at least one downcast.

[18] The sheer volume of the CTD data set required a technique for automatically identifying profiles that were degraded by measurement problems. Raw temperature and conductivity data from the CTD sensors (recorded at 24 Hz) were averaged in 0.1 m vertical bins. A series of correlation and regression coefficients were formed between the temperature and conductivity profiles measured by the two sensor pairs for each downcast and between sequential downcasts for each of the sensor pairs. These statistics were then used to identify downcasts for which one or both sensor pairs had unacceptably large noise levels and/or offsets. Of the 12,350 downcasts recorded, 11,013 (89%) were determined to have high-quality temperature and conductivity data for at least one sensor pair. Salinity and density were calculated from temperature and conductivity using standard formulations. Individual vertical profiles of potential temperature T , salinity S , and potential density ρ (referenced to surface pressure) from each downcast were then ensemble averaged over the 3-h periods.

[19] Descriptive statistics derived from the CTD observations include properties that characterize the heat content of the well-mixed surface layer and the heat content and stratification of the layer just below the mixed layer where entrainment processes were active. Mixed layer values of temperature, salinity, and density, denoted by a subscript ml , were defined as vertical averages over the depth range 10 to 15 m. This depth range represented properties of the upper part of the typically turbulent ocean mixing layer that were sampled near the upper depth limit of the CTD system. The departure from freezing near the ice-ocean interface, $\delta T_{ml} = T_{ml} - T_{fp}(S_{ml})$ where T_{fp} is the freezing point as a function of salinity, was calculated from the surface values. A robust estimate of the thickness of the well-mixed surface layer, h_{ml} , was defined by the depth where density increased from its surface value to 20% of the difference between 100-m and surface values. This definition is effective, because there is typically a density step at the base of the mixed layer, but the magnitude of the step varied seasonally in the data set. In the remainder of the paper, the terms surface mixed layer and IOBL will be used somewhat interchangeably, recognizing that the mechanical boundary layer is typically contained within the layer we refer to as the mixed layer. An “entrainment layer” was defined as the area just below the well-mixed layer that was likely to be exposed to IOBL entrainment during strong surface forcing events. On the basis of microstructure measurements (described below), the thickness of the entrainment zone during strong forcing events is on the order of 5 m, and so the entrainment layer is taken as a 5-m-thick zone underlying the surface layer. Statistics describing the entrainment layer are denoted by a subscript pyc . For example, stratification was characterized as the salinity difference across the layer, ΔS_{pyc} , and heat content was

characterized using the average departure of temperature from freezing in the layer, δT_{pyc} . While these criteria are subjective, the values chosen work well for the range of conditions encountered and highlight the features of interest to us here, and results are not significantly different using other, reasonable values of the criteria.

2.2. Thermal Microstructure

[20] The measurement of thermal microstructure was chosen to characterize turbulence transport rates from the profiler package because of the requirement that the system run with a minimum of supervision and repairs over the yearlong duration of the program. For example, velocity microstructure measurements would have been contaminated by mechanical vibrations of the winch, and conductivity measurements would likely have been interrupted frequently by biofouling and damage to the delicate fast conductivity sensors that resolve dissipation scales.

[21] Output from two fast response, glass-coated-bead thermistors (Thermometrics FP07) was preemphasized [e.g., *Mudge and Lueck*, 1994], antialias filtered, and sampled to 16 bit resolution at 188 Hz. Upon analysis, the preemphasized data were deconvolved into the original signal and its derivative. For each downcast, temperature calibrations were obtained by regression against CTD temperature and a spectral noise model was estimated using the most quiescent sections of the cast (typically near the bottom). Casts containing high-quality data were identified with a regression/correlation coefficient analysis between sensors and casts analogous to that used to clean up the CTD data set, with an additional criterion that the variance of the noise floor model not be too large. 51% of the 3-h ensemble periods had at least three downcast profiles with high-quality data. Heat flux estimates were not attempted for ensemble periods with fewer than three downcasts.

[22] The fundamental quantity estimated from the thermal microstructure observations is the rate of dissipation of turbulent thermal variance, defined by

$$\chi = 6\kappa_T \overline{\left(\frac{dT'}{dz}\right)^2} \quad (1)$$

for one-dimensional measurements in an assumed isotropic turbulent field. Here, κ_T is the molecular diffusivity of heat, dT'/dz is the vertical derivative of the turbulent temperature field, and the overline notation indicates temporal averaging. The temporal measurements are translated into spatial measurements along the vertical profile using Taylor’s frozen turbulence hypothesis in which sensor fall speed u_{drop} and the ice drift speed V_{ice} are included in an effective advection speed

$$\frac{dT'}{dz} = \frac{dT'}{dt} \left(u_{drop}^2 + V_{ice}^2\right)^{-1/2}. \quad (2)$$

The variance of dT'/dz was estimated spectrally, with corrections applied for the response of a glass bead–type thermistor [e.g., *Fleury and Lueck*, 1994] and sensor noise. Spectral points with frequency greater than the 1/5-power point of the of the transfer function (at about 25 Hz) were discarded. This frequency cutoff translates into a maximum

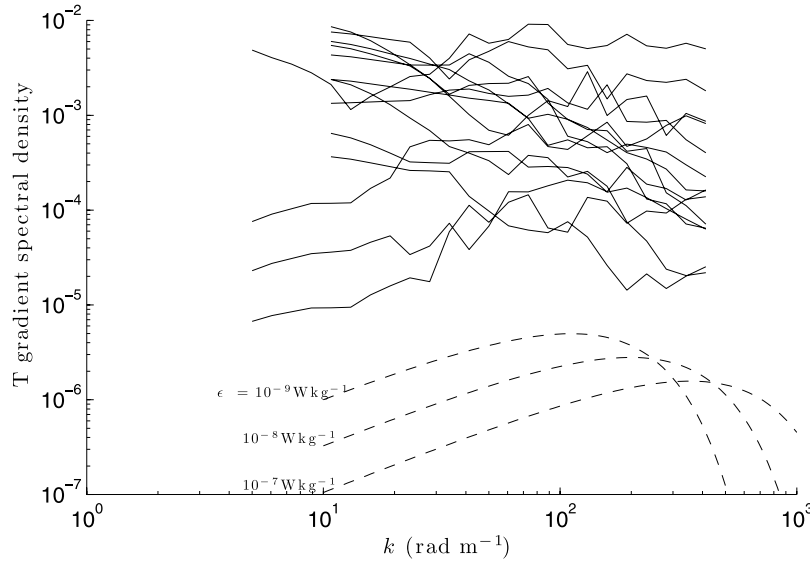


Figure 2. Example of 3-h ensemble-averaged temperature gradient spectra from an FP07 thermistor during a period of strong entraining heat fluxes at the end of yearday 430. The Batchelor spectral form for three values of ϵ are plotted for comparison.

resolvable wave number that decreases from $k_{\max} = 467 \text{ rad m}^{-1}$ for motionless ice to $k_{\max} = 380 \text{ rad m}^{-1}$ for ice moving at 0.25 m s^{-1} ; unfortunately, the spatial resolution was most limited for fast moving ice (i.e., strong surface forcing).

[23] The technical difficulty of fully resolving the temperature dissipation spectrum in energetic turbulent fields with thermistors is well known [e.g., *Gregg, 1999*]. The Batchelor model of the temperature dissipation spectrum predicts an exponential roll-off at the Batchelor wave number

$$k_B = \left(\frac{\epsilon}{\nu \kappa_T^2} \right)^{1/4}, \quad (3)$$

where ν is molecular kinematic viscosity, and ϵ is the dissipation rate of turbulent kinetic energy (TKE). On the basis of the maximum resolved wave number in the observed spectra and (3), we expect that the FP07 thermistors were unable to completely resolve $\left(\frac{dT}{dz} \right)^2$ if ϵ was greater than about $10^{-9} \text{ W kg}^{-1}$. Examples of temperature gradient spectra near the base of the mixed layer from a period of strong surface forcing ($u_{*0} = 0.01 \text{ m s}^{-1}$) on yearday 431.0 (Figure 2) illustrate the resolution problem. (The term “yearday” is taken to mean fractional day of the year, beginning 1 January 1997. Yearday values extend continuously into 1998, with noon on 1 January 2008 taking yearday value 366.5.) Most of these spectra do not contain clear maxima or signs of exponential roll-off, indicating that ϵ in this particular instance was greater than at least $10^{-8} \text{ W kg}^{-1}$ (by comparison of the observed spectra to the theoretical Batchelor forms plotted in the Figure 2). Because the spectral peaks occur beyond the maximum observed wave number, the spectra by themselves cannot be used to estimate the fraction of variance that went unresolved by the thermistors.

[24] In order to estimate and correct for the unresolved variance of the thermistor measurements, we have used the results of the SLTC model (section 3) to infer ϵ , which provides the additional information required to calculate the

amount of variance beyond k_{\max} in the observed spectra. The SLTC model is a first-order turbulence closure model, which means it does not carry an equation for TKE, but ϵ can be estimated from the SLTC results by assuming a local balance between TKE production and dissipation. Using the turbulent diffusivity of momentum ν_T and diagnosed horizontal velocity output from the model, the SLTC estimate of ϵ is

$$\epsilon^{SLTC} = \nu_T \left[\left(\frac{\partial u}{\partial z} \right)^2 + \left(\frac{\partial v^2}{\partial z} \right) \right]. \quad (4)$$

After ϵ^{SLTC} is converted to a Batchelor wave number using (3), the ratio k_B^{SLTC}/k_{\max} determines the fraction of unresolved variance in any particular observed spectrum, assuming that the measured spectra follow the theoretical Batchelor form. Figure 3a illustrates that k_B^{SLTC} was several times larger than k_{\max} during strong storm events. For ensembles with $u_{*0} > 0.01 \text{ m s}^{-1}$, the average value of k_B^{SLTC} was 1347 rad m^{-1} , 3.2 times the average value of k_{\max} , 800 rad m^{-1} . A corresponding χ “correction factor” (Figure 3b), which corrects for the estimated unresolved variance, has an average value of 2.6 during strong forcing conditions and it has maximal values in the range 3–7 for the largest storms encountered. In reality, some fraction (about 20% [e.g., *Osborn, 1980*]) of the TKE is lost to buoyancy production, which implies that both the estimated ϵ and the calculated correction factor represent upper limits of the actual values. We apply this correction factor to the spectral χ estimates and use the difference between the corrected and uncorrected forms as a measure of uncertainty.

[25] As noted above, the main use here for the thermal microstructure data is to estimate the heat flux across the base of the well-mixed surface layer as a quantification of the amount of heat entering the surface layer from the upper pycnocline. Heat flux is estimated from χ using the method of *Osborn and Cox [1972]*, in which a balance is assumed

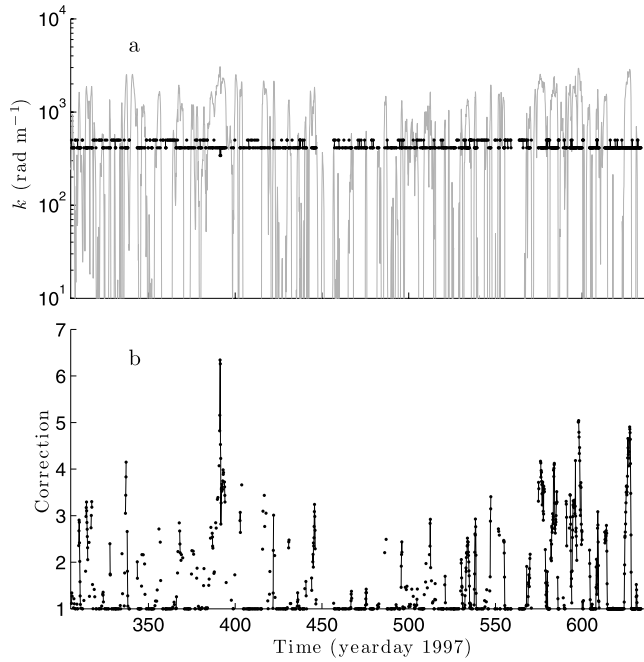


Figure 3. (a) Time series of the maximum resolvable vertical wave number with the FP07 thermistors (black) and Batchelor wave number at the base of the mixed layer estimated from the SLTC model results (gray). (b) The corresponding correction factor that is applied to the thermistor χ estimates. The maximum resolved wave number is a function of advection speed. The values in the plot are discretized because logarithmic averaging was applied to the observed spectra, with the result that the high/low values correspond to slower/faster ice speeds.

to hold between the production and dissipation of turbulent temperature variance

$$-\overline{T'w'} \frac{dT}{dz} = \frac{1}{2} \chi. \quad (5)$$

Combining (1) and (5), the microstructure-based heat flux estimate is

$$\overline{T'w'} = 3\kappa_T \frac{\overline{(dT'/dz)^2}}{dT/dz}, \quad (6)$$

where κ_T is set to a constant value of $1.4 \times 10^{-7} \text{ m}^2 \text{ s}^{-1}$. This estimate is essentially determined by the ratio of the temperature gradient variance to the mean, or background, temperature gradient dT/dz . In an episodically energetic and vertically structured environment such as the mixed layer base and upper pycnocline, it is difficult to characterize average values of these two quantities, especially with a sensor moving in the vertical direction. Extensive vertical averaging is not possible at the approximately 1-m scale required to resolve the vertical structure near the base of the mixed layer and within the entrainment layer. Also, h_{ml} is constantly changing because of internal wave motions and the temperature gradient inferred from a single profile at these small scales is not representative of the background profile if turbulence is active.

[26] A procedure of careful vertical averaging within individual profiles and ensemble averaging over the 3-h periods was used to produce sensible estimates of the background temperature gradient and stable estimates of χ . For each downcast, vertical averaging bins were set up with respect to the depth of the mixed layer base, defined by h_{ml} , for that profile so that the vertical bins were effectively tracking the base of the mixed layer. 2.5-m-thick bins were used above the base of the mixed layer and 1-m-thick bins were used below the mixed layer base, within the entrainment layer. Larger bins were used within the mixed layer to aid in the resolution of extremely small temperature gradients. Smaller vertical bins were used in the pycnocline to allow as much resolution as possible of the highly variable vertical structure there. Within each bin, spectral estimates of the variance of dT'/dz were calculated and values of dT/dz were stored. These vertically averaged results were then ensemble averaged over all of the downcasts within each 3-h period to produce mean quantities $\overline{(dT'/dz)^2}$ and $\overline{dT/dz}$. After this ensemble averaging, the ratio $\overline{(dT'/dz)^2}/\overline{dT/dz}$ is formed for the calculation of heat fluxes using (6). Ensemble averaging of $\overline{(dT'/dz)^2}$ and $\overline{dT/dz}$ before calculating their ratio reduces variability of the heat flux estimates. The vertical average of the ensemble-averaged heat flux estimates over a 10-m-thick interval centered on the mixed layer base is taken as the final estimate of pycnocline heat flux F_{pyc} . Occasionally, the temperature gradient is too small to be accurately resolved. In order to avoid spurious flux estimate caused by unresolved gradients, bins with $\overline{dT'/dz} < 10^{-3} \text{ K m}^{-1}$ are excluded from the final vertical average. It is physically reasonable to exclude these points, because (as described below) the Osborn-Cox model probably does not work well for extremely well-mixed regions.

[27] The averaging method is illustrated using the example from yearday 431.0 (Figure 4) that was introduced above. The average depth of the mixed layer over the ten profiles that compose this ensemble was about 29 m. The temperature gradient in the lower portion of the surface layer was small but measurable with $\overline{dT'/dz} > 10^{-3} \text{ K m}^{-1}$. Temperature gradient variance was above the noise level throughout the bottom of the mixed layer and the upper pycnocline layer. As expected, there is significant variability in the temperature gradient and temperature gradient variance between profiles; but the ensemble averages of these quantities (which are used for $\overline{dT'/dz}$ and $\overline{(dT'/dz)^2}$ in (6) as described above) are well behaved and produce physically reasonable estimates of heat flux (Figure 4). The vertical extent of the entrainment zone, taken as the area below the mixed layer base where heat flux is significantly greater than zero, is about 6 m. The uncorrected heat flux estimates increase from near zero at the bottom of the entraining layer to greater than 15 W m^{-2} at the base of the mixed layer. The heat flux continues to increase with decreasing depth within the mixed layer in this example, with a maximum value of nearly 60 W m^{-2} . The uncertainty of the mixed layer estimates is relatively large because of large variability in the temperature gradient estimates there. There is also the possibility that the mixed layer estimates are biased large because of the potential significance of turbulent advection in the temperature variance budget away from the region of strong gradient below the mixed layer base [e.g., Shaw et al., 2001]. The correction factors for unresolved

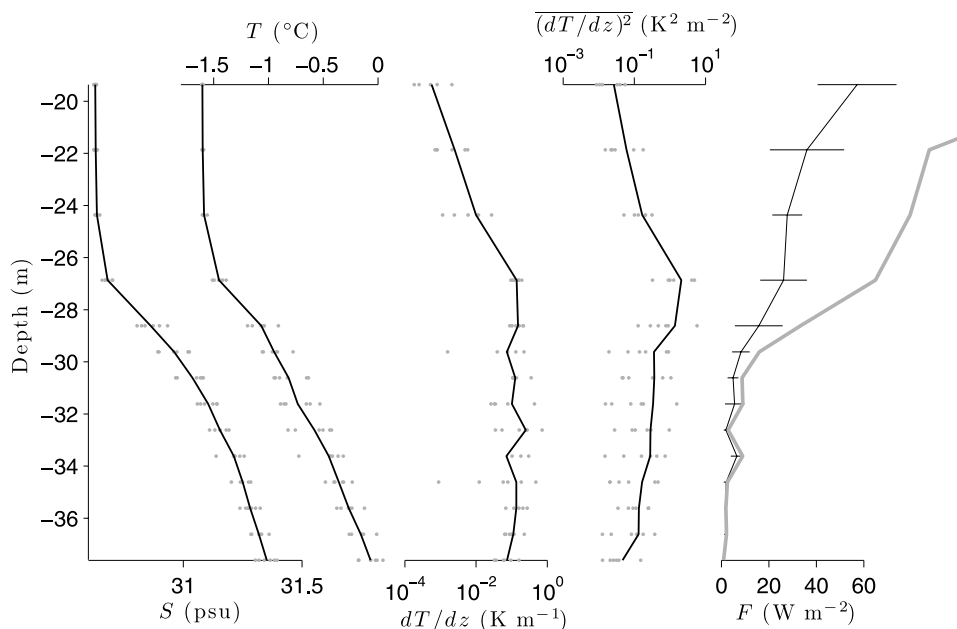


Figure 4. Example of the ensemble-averaging procedure used to estimate heat flux using the thermal microstructure data. This 3-h ensemble is from a period of strong entraining heat fluxes at the end of yearday 430. Each of the ten profiles (gray dots) that contribute to this ensemble (black lines) is vertically shifted so that the mixed layer depth in each profile occurs at the ensemble average mixed layer depth (29.0 m). In the heat flux plot, the black and gray lines correspond to the uncorrected and corrected χ estimates, respectively.

variance range from 2.8 for the top bin, where ϵ is greatest, to 1.0 at the bottom bin. The vertical average of the variance-corrected, ensemble heat fluxes over the 10-m range centered in the base of the mixed layer provides a pycnocline heat flux estimate of $F_{pyc} = 40.1 \text{ W m}^{-2}$.

2.3. Turbulence Instrument Clusters

[28] The vertical array of turbulence sensors consisted of sensitive mechanical current meters and nearly collocated temperature and conductivity sensors (see *McPhee* [2002] for details). Individual sets of instruments, known as Turbulence Instrument Clusters (TIC), were mounted on a rigid mast suspended below the ice to form a vertical array of between two and four clusters. During the first half of the experiment (before the forced relocation described above) four TICs were deployed at nominal depths of 4, 8, 12, and 16 m below the ice undersurface. For the second half of the experiment two TICs were deployed at nominal depths of 4 and 8 m. The TIC sensors were sampled at 6 Hz, resolving the energy-containing turbulence scales in the IOBL and allowing direct, eddy correlation estimates of turbulent fluxes of momentum and heat. Covariance estimates were calculated from fluctuations over 15-min averaging periods and the resulting fluxes were further averaged over the 3-h ensemble periods. Previous results using the system demonstrate that fluxes based on 3-h-averaging periods are highly reliable. Of the 354 days spanned by CTD operations, at least one 3-h ensemble was available from the TICs for 188, 231, 84, and 62 days, respectively with increasing cluster depth. The average number of ensembles per day with at least one ensemble was four for the shallowest sensor and five for the others. There were 108 days for which there were no ensembles available from any of the clusters. The larger

number of days without TIC data (relative to profiler data) is due to a minimum flow speed requirement of the mechanical current meters. During summer, biofouling of the mechanical current meters was a problem, necessitating regular retrieval and redeployment of the TICs to allow for cleaning. Heat flux estimates from the nominal 8-m depth level, F_{8m} , were taken to represent heat fluxes within the IOBL.

3. SLTC Model

[29] The steady local turbulence closure model [*McPhee*, 1999] assumes that turbulence adjusts instantaneously to ice/ocean interface flux conditions and to a prescribed density structure in the upper ocean. It utilizes an iterative scheme that begins by solving the IOBL momentum equation (without local inertia) following similarity scaling that takes into account both interfacial stress and buoyancy flux [*McPhee*, 1981], but assumes no stratification in the upper ocean. Given a first estimate of IOBL shear and turbulence scales (hence eddy diffusivity), profiles of heat and salt flux are calculated from the prescribed temperature and salinity structure. In the next iteration, the calculated IOBL buoyancy flux is included in a new eddy viscosity calculation, and the momentum equations are solved again. This is repeated until the difference between successive iterations is small enough to meet a convergence criterion. By including buoyancy flux throughout the IOBL, the model can account, e.g., for a relatively shallow well-mixed layer where stress near the top of the pycnocline is an important element of the overall momentum structure. Fluxes across the ocean-ice interface are determined with a three-equation interface submodel [*McPhee et al.*, 2008]. The advantage of the SLTC over time-dependent numerical models with similar or analogous closure is that it

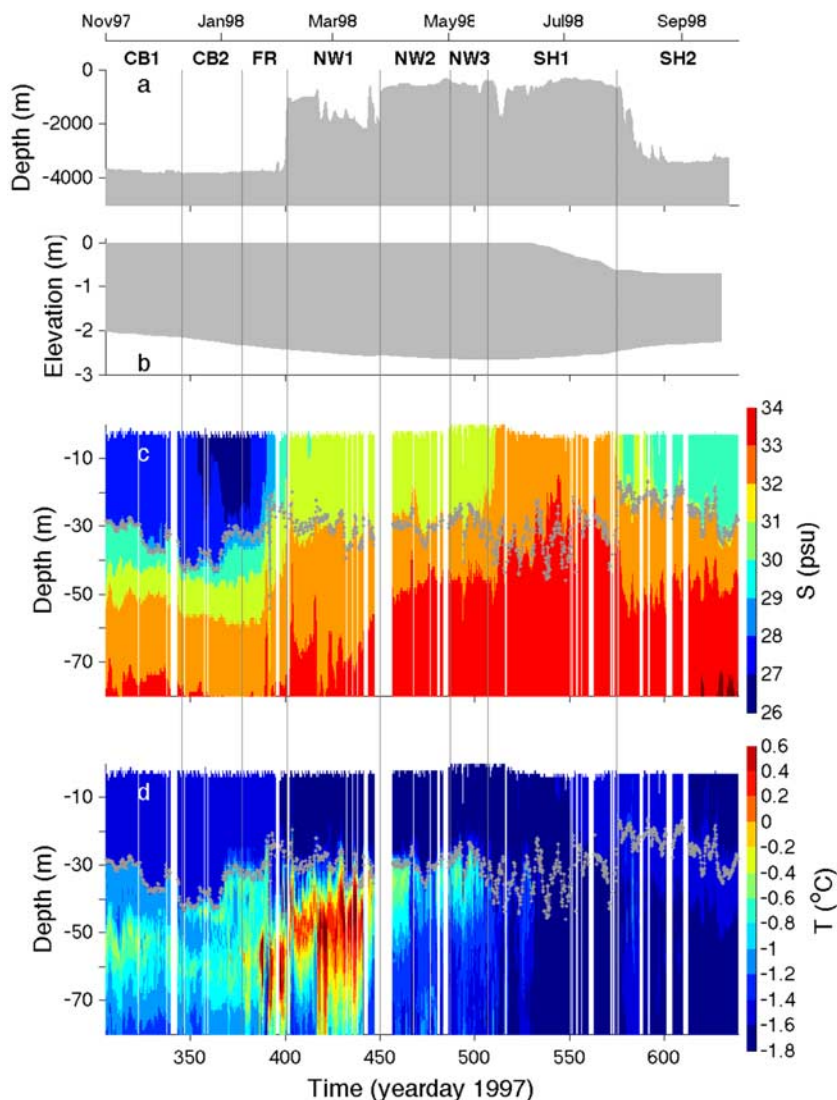


Figure 5. Time series of (a) water depth and (b) elevations of the top and bottom surfaces of the ice cover and time-depth sections of (c) salinity and (d) potential temperature along the SHEBA ice camp drift. Averaged measurements of ice surface and bottom elevation from the “Pittsburgh” site are used to illustrate the evolution of ice thickness in Figure 5b. Mixed layer depth is indicated by the gray curves in the salinity and temperature sections. Vertical lines mark the boundaries between the “segments” described in the text.

can be applied to a particular measured profile of temperature and salinity within a data set.

[30] The SLTC model was solved using observed ice velocity, ice thickness and temperature (to determine the interface buoyancy flux), and vertical profiles of CTD temperature and salinity for each 3-h ensemble. Inertial, and possibly tidal, components were removed from the ice velocity time series by complex demodulation. Estimates of temperature gradient in the lower ice column come from the thermistor records of ice observation station “Pittsburgh” [Perovich *et al.*, 2003]. For ensembles with no CTD profiles, temperature and salinity were interpolated linearly between adjacent 3-h averages for which there were at least two up and down profiles. The only period where interpolation of CTD profiles significantly affects the SLTC modeling is during the 9-day-long period

between days 447 and 455 (discussed further in section 4.3) for which CTD data are unavailable because of the relocation of the ocean measuring systems. The surface roughness length z_0 , taken equal to 0.049 m, was estimated by optimizing agreement between SLTC model and observed current and stress at the 8-m TIC [McPhee, 2008, chapter 9]. The quality of the resulting surface stress estimate depends on the assumptions that (1) the z_0 value is representative of the entire floe for the duration of the project and (2) over the long drift the average value of geostrophic (sea surface tilt) current is near zero.

[31] For comparison with and supplementation of the observation-based flux estimates, continuous time series of the interface friction speed, u_*0 , and heat fluxes at the ocean-ice interface, the depth of the nominal 8-m TIC, and the depth of the mixed layer base (averaged over the same 10-m vertical

Table 1. Summary Statistics for the Drift Segments Discussed in the Text^a

Yearday	h_{ml}^b (m)	S_{ml}^c (psu)	ΔS_{pyc}^d (psu)	δT_{ml}^e (K)	δT_{pyc}^f (K)	F_{pyc}^g ($W m^{-2}$)		F_0^h ($W m^{-2}$)	$F_0 - F_\epsilon$ ($W m^{-2}$)	$\frac{dE_b}{dt}^i$ ($W m^{-2}$)	
						SLTC	μT				
CB1	305–346	32.7	27.7	0.9	−0.00	0.47	2.1 (2.6)	0.3–0.6	0.3	−11.2	−10.8
CB2	346–377	37.5	26.8	1.4	−0.00	0.60	−0.0 (0.2)	0.0–0.0	0.1	−15.8	−19.0
Basin	305–377	34.8	27.3	1.2	−0.00	0.53	1.2 (1.6)	0.2–0.3	0.2	−13.2	−14.4
FR	377–401	30.5	27.9	0.8	0.01	0.53	4.4 (9.3)	0.4–1.2	2.0	−12.5	−13.4
NW1	401–450	30.3	30.4	0.3	0.02	0.83	3.8 (5.5)	3.5–5.7	4.3	−9.9	−10.3
NW2	450–487	30.3	30.9	0.3	0.01	0.73	0.7 (0.6)	1.7–1.8	2.1	−7.7	−7.4
NW3	487–507	28.4	30.6	0.4	0.03	0.69	0.5 (0.7)	0.8–0.9	3.8	−3.0	−2.2
Northwind	401–507	29.8	30.6	0.3	0.02	0.76	2.1 (3.2)	2.5–3.7	3.5	−7.8	−7.8
SH1	507–575	33.2	31.5	0.2	0.11	0.16	0.1 (0.1)	−0.1–0.1	18.3	15.7	8.6
SH2	575–640	24.9	29.8	0.7	0.06	0.24	3.1 (3.7)	0.2–0.7	14.1	14.2	14.0
Summer	507–640	28.4	30.5	0.5	0.08	0.21	1.5 (2.5)	0.1–0.4	16.3	14.9	11.1
Annual	305–640	30.0	29.8	0.6	0.05	0.43	1.8 (2.9)	0.7–1.2	7.6	−0.7	−2.4

^aAlso shown are combined statistics for the Canada Basin (segments CB1 and CB2), Northwind Rise Area (NW1, NW2, and NW3), the summer heating period (SH1 and SH2), and the entire annual cycle.

^bMixed layer depth.

^cMixed layer salinity.

^dSalinity difference across the entrainment layer.

^eMixed layer departure from freezing.

^fEntrainment layer departure from freezing.

^gEntrainment layer heat flux. For the pycnocline heat fluxes, the number in parentheses in the SLTC column is the average value over only those segments for which a microstructure-based estimate was available, and for the microstructure column the range of values is based on using the uncorrected and corrected values of χ .

^hOcean-ice interface heat flux.

ⁱIce base energy budget tendency.

interval as the microstructure estimate) were extracted from the 3-h SLTC results. The interface SLTC fluxes are expected to be more accurate than estimates based on Rossby similarity theory and bulk heat transfer laws because the SLTC model includes physics missing from Rossby similarity theory and the bulk heat transfer law (namely buoyancy effects resulting from the stratified water column and the surface buoyancy flux and a more realistic interface model that accounts for rate limiting effects of salt transport).

4. Upper Ocean Stratification, Heat Content, and Heat Flux

[32] The SHEBA ice camp field program began near the center of the Canada Basin on 12 October 1997 (1997 yearday 285; Figure 1). Measurements were obtained for the next 353 days as the camp drifted anticyclonically in the Beaufort Gyre, covering a total distance of 2762 km. The program completed on 30 September 1998 (1997 yearday 638) over the Mendeleev Abyssal Plain, 744 km from the initial location. Over the course of the drift, upper ocean conditions were strongly affected by the underlying bathymetry and the seasonal cycle in atmospheric radiation.

[33] The camp drifted over the irregular and steeply sloping western boundary of the Canada Basin, known as the Chukchi Borderlands, between February and August 1998 (1997 yeardays 401–575, Figures 1 and 5a). Water depth below the camp decreased from more than 4000 m in the center of the Canada Basin to less than 1000 m over the Borderlands. The drift track crossed the Northwind Ridge and Northwind Abyssal Plain nearly perpendicular to the axis of the ridge and continued on across the Chukchi Shelf. Over the Chukchi Shelf, the drift track turned north and the camp crossed the “gap” separating the Chukchi Shelf from the Chukchi Plateau. Strong spatial fronts overlying the outer flanks of the Northwind Ridge in sections of salinity and temperature from the CTD profiler (Figures 5c and 5d)

illustrate the strong control on ocean circulation provided by the bathymetry of the Chukchi Borderlands: upper pycnocline stratification decreased and upper pycnocline heat increased as the front was crossed.

[34] Ice thickness measurements from the “Pittsburgh” ice mass balance site [Perovich *et al.*, 2003] document ice growth from the beginning of the observation period until yearday 520 (4 June 1998) and melt at the bottom of the ice from then until the end of the record (Figure 5b). Surface ice melt began slightly later, yearday 530 (14 June 1998), although snow melt had begun earlier. The development of the summer 1998 mixed layer is evident in the evolution of salinity field around yearday 575 (Figure 5c, as the camp, coincidentally, drifted off of the Chukchi Shelf). Freshwater from ice and snow melt formed a thin, fresh surface layer and a strongly stratified upper pycnocline.

[35] Although the ocean observations are thus complicated by a combination of geographic and seasonal variability, fortuitously, the record can be divided into contiguous segments for which the spatial and seasonal variations are mostly separable. Boundaries between the segments were defined on the basis of the positions of spatial fronts and on the onset of basal melting and the development of the summer mixed layer during the heating season. The one exception to this principle is the portion of the drift encompassing the strong front above the eastern flank of the Northwind Ridge described above; this part is taken as a segment unto itself. The time ranges of the segments are listed in Table 1 and are indicated on the map of Figure 1. Briefly, we defined two segments over the Canada Basin, denoted “CB1” and “CB2,” in which the surface layer was close to an ice bath and the entrainment layer contained relatively little heat compared to the other segments. These were followed by a segment, denoted “FR,” that contained the strong front. Three segments were placed over the Northwind Ridge, Northwind Abyssal Plain and Chukchi Shelf, denoted “NW1,” “NW2” and “NW3”; these were characterized

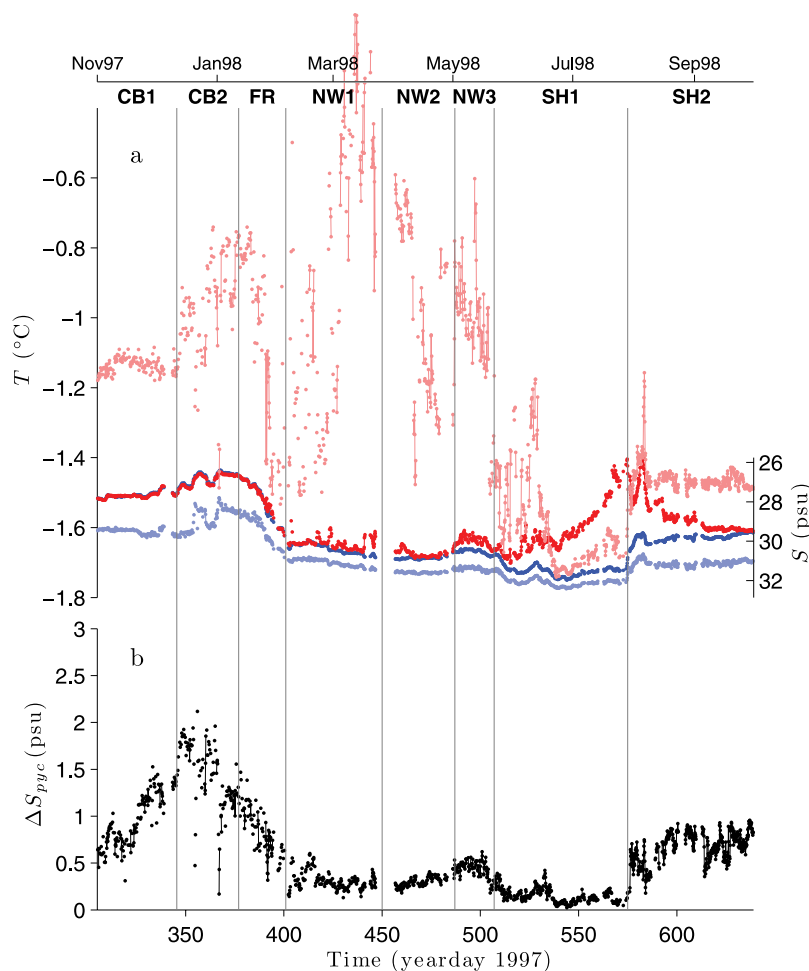


Figure 6. Time series of descriptive statistics. (a) Mixed layer potential temperature (dark red) and salinity (dark blue) and entrainment layer potential temperature (light red) and salinity (light blue). The salinity axis on the right is aligned with respect to the temperature axis so that freezing point temperature corresponding to a particular salinity value can be read off of the temperature scale on the left and the departure from freezing for either layer is the distance between the temperature curve and the freezing point curve. (b) Salinity difference across the entrainment layer. Vertical lines mark the boundaries between the “segments” described in the text.

by weak entrainment layer stratification, large entrainment layer heat content, and surface temperatures intermittently above the freezing point. We think that solar radiation started penetrating to the upper ocean during NW3. The onset of the melting season was nearly coincident with an upper ocean front (located at the northern edge of the Chukchi Shelf) across which heat disappeared from the upper pycnocline, so that heat transport in the upper ocean during summer was dominated by radiative forcing. We divided the summer heating season into two segments, denoted “SH1” and “SH2,” for a grand total of eight segments.

[36] Detailed descriptions of the stratification, heat content, and heat fluxes across the IOBL within each of the drift segments are presented in the following subsections. We are dependent on the SLTC results for interface heat and momentum fluxes. There are differences between the observed and SLTC estimates of F_{8m} and F_{pyc} , so both versions of these estimates are discussed. Values of microstructure F_{pyc} are quoted as a range, using the uncorrected and corrected versions as lower and upper limits. The presentation is based

on the time-depth sections of salinity and potential temperature (Figures 5c and 5d), time series of the descriptive CTD statistics described in section 2.1 (Figure 6), vertical profiles of departure from freezing and salinity (Figure 7), and time series of interface friction speed u_{*0} and the heat flux estimates F_0 , F_{8m} , and F_{pyc} (Figures 8–10). Figure 6a contains the mixed layer and entrainment layer values of potential temperature, freezing temperature, and salinity. The boundaries between the drift segments are indicated in Figures 5, 6, and 8–10, and segment-averaged values of the statistics are listed in Table 1.

4.1. Canada Basin

[37] Upper ocean conditions measured near the center of the Canada Basin upon the establishment of the camp came as a surprise: surface salinity was fresher and pycnocline heat content was larger than seen in previous observations. Over segment CB1 (yearday 305–326), the mixed layer was 30 m deep on average, was nearly an ice bath (T_{ml} within a few mK of the freezing point), and had average salinity $S_{ml} =$

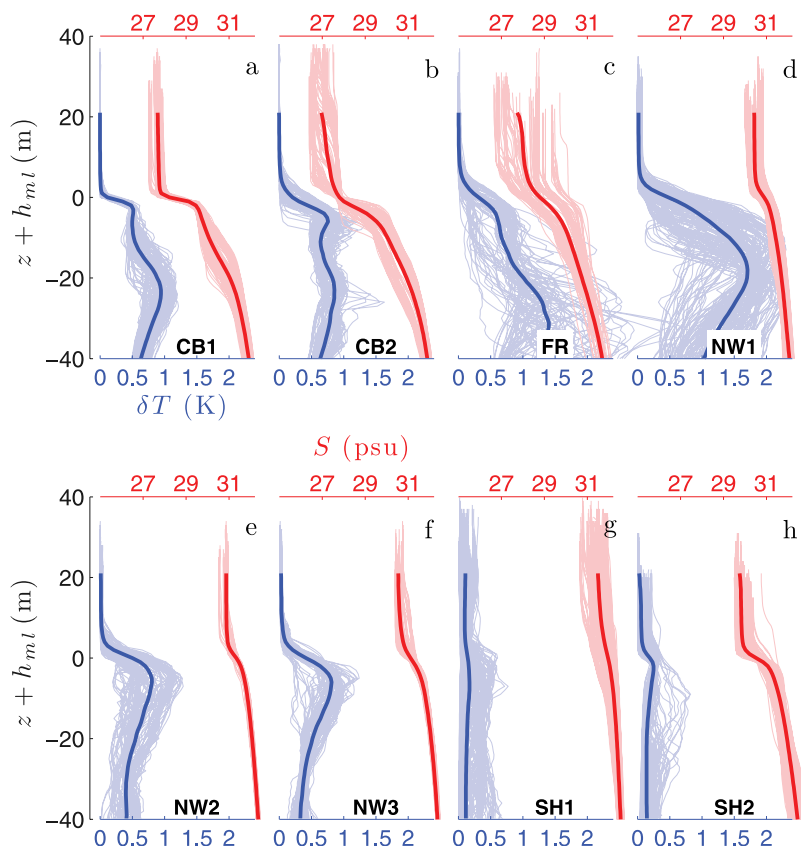


Figure 7. Vertical profiles of 3-h temperature departure from freezing (blue) and salinity (red) for the eight segments discussed in the text. Profiles are plotted with respect to the depth of the base of the mixed layer, $z + h_{ml}$. Thick lines in each of the plots are segment-averaged profiles, again with respect to h_{ml} . Segments (a) CB1, (b) CB2, (c) FR, (d) NW1, (e) NW2, (f) NW3, (g) SH1, and (h) SH2.

27.7 psu. The entrainment layer was strongly stratified with a salinity difference $\Delta S_{pyc} = 0.9$ psu. The stratification was formed by a 0.67 psu m^{-1} salinity gradient, the largest gradient in the record. The upper pycnocline contained heat in two distinct temperature maxima (Figures 5d and 7a). The shallower one was found at depth 33 m, at salinity 29.4 psu, and had temperature maximum -1.15 C. The deeper one was found at depth of about 55 m, at salinity 31.0 psu, and had temperature maximum -0.60 C. The deeper maximum lay below the defined entrainment layer so that only the shallow one contributed to δT_{pyc} . Compared to the 1975 AIDJEX measurements, *McPhee et al.* [1998] noted that CB1 surface salinity was anomalously fresh (27.8 psu compared to 29.7 for AIDJEX) and that CB1 pycnocline heat content was anomalously large (δT_{pyc} 2.5 times AIDJEX). *McPhee et al.* [1998] also estimated that the vertical structure of the CB1 salinity profile required 2 m of freshwater input. Using $\delta^{18}\text{O}$ as a tracer in addition to salinity, *Kadko and Swart* [2004] find that the freshening was derived from a large ice melt (1.2 m) with a significant contribution from river runoff (0.8 m). On the basis of model results and the tracer ^7Be , *Kadko* [2000] concluded that the heat in the shallow temperature maximum was emplaced during the 1997 heating season.

[38] Upper ocean structure was modified by the appearance of even fresher mixed layer water as the camp moved

southwestward away from the center of the Canada Basin during segment CB2 (days 327–367). The minimum of S_{ml} was 26.4 psu and the segment-averaged value was 26.8 psu, the lowest segment average of the record (Table 1). This near-surface front (salinity structure below the entrainment layer did not change appreciably, Figure 7b) was encountered about 130 km from the eastern edge of the Northwind Ridge (Figure 1). The fresh water was not uniformly mixed throughout the surface layer, as salinity and temperature gradients extended, intermittently, almost to the surface (Figure 7b). This variability in the vertical density structure caused h_{ml} estimates to vary between 15 and 30 m (Figures 5c and 5d). There was little heat associated with this fresh water, as T_{ml} remained at the freezing point (Figure 6a). The two subsurface temperature maxima observed in CB1 were continuous across the front between CB1 and CB2. Within CB2, the heat content of the shallower temperature maximum was related to the freshwater content of the surface layer, both increased through most of the segment. δT_{pyc} had an average value of 0.60, larger than observed during CB1. The vertical extent and heat content of the deeper temperature maximum grew larger at the end of CB2 (Figures 5 and 7b), but these changes occurred below the entrainment layer and did not contribute to δT_{pyc} . The freshening surface layer caused the stratification of the entrainment layer to strengthen: average and maximum values of ΔS_{pyc} over CB2 were 1.3

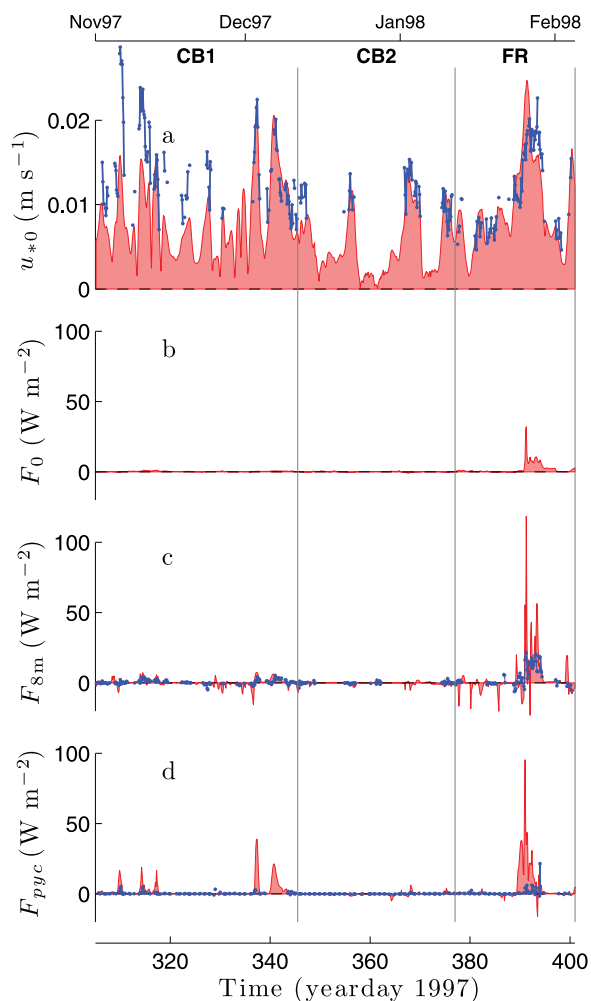


Figure 8. Time series of (a) interface friction speed u_{*0} , (b) interface vertical heat flux F_0 , (c) vertical heat flux at 8-m depth F_{8m} , and (d) vertical heat at the base of the mixed layer F_{pyc} for segments CB1, CB2, and FR. Observational (blue) and SLTC model (red) estimates are plotted. Vertical lines mark the boundaries between the “segments” described in the text.

and 2.1 psu, the largest such values observed (Figure 6). The upper ocean conditions of CB2 were even more anomalous than those measured during CB1.

[39] Although there were ample amounts of heat in the Canada Basin entrainment layer, the mixed layer was nearly an ice bath throughout CB1 and CB2, indicating that vertical transport from this layer must have been weak. Indeed, heat flux estimates across the IOBL were uniformly small for the two Canada Basin segments (Figure 8). Segment-averaged values of F_0 were 0.3 and 0.1 W m^{-2} for CB1 and CB2, respectively. Observed and SLTC heat fluxes within the surface layer were also small. During CB1, average TIC and SLTC values of F_{8m} were 0.5 and 0.2 W m^{-2} , respectively. During CB2, segment-averaged TIC and SLTC F_{8m} were actually slightly negative, -0.1 and -0.4 W m^{-2} , respectively, as a result of the vertical structure associated with the front which created a negative near-surface temperature gradient. Interestingly, there is poor agreement between the model and microstructure-based estimates of

F_{pyc} during these strongly stratified conditions. For example, there were four storm-forced entrainment events during CB1 for which u_{*0} exceeded 0.01 m s^{-1} and that were resolved well by microstructure observations. During these events, SLTC F_{pyc} were 3–5 times larger than the observational estimates (Figure 8d). This is reflected in the average values of F_{pyc} for CB1: 2.1 and 0.3–0.6 W m^{-2} for model and observation, respectively. The average SLTC F_{pyc} value for only those periods that had microstructure estimates available was 2.6 W m^{-2} . The agreement between observation and model is better during CB2 (Table 1), but probably only because there were no large surface forcing events during that segment. The SLTC F_{pyc} may be inaccurate during these segments, because these estimates are much larger than observed and modeled F_{8m} and F_0 and because there was no observed warming of the surface layer (Figure 6a). Although there was an increase in the upper halocline heat content associated with the fresher surface layer of CB2, the front between CB1 and CB2 did not affect significantly ocean heat flux, probably because the warming of the upper halocline layer was accompanied by stronger stratification. Overall, the insulating effect of the strong stratification provided a very effective capping of the heat

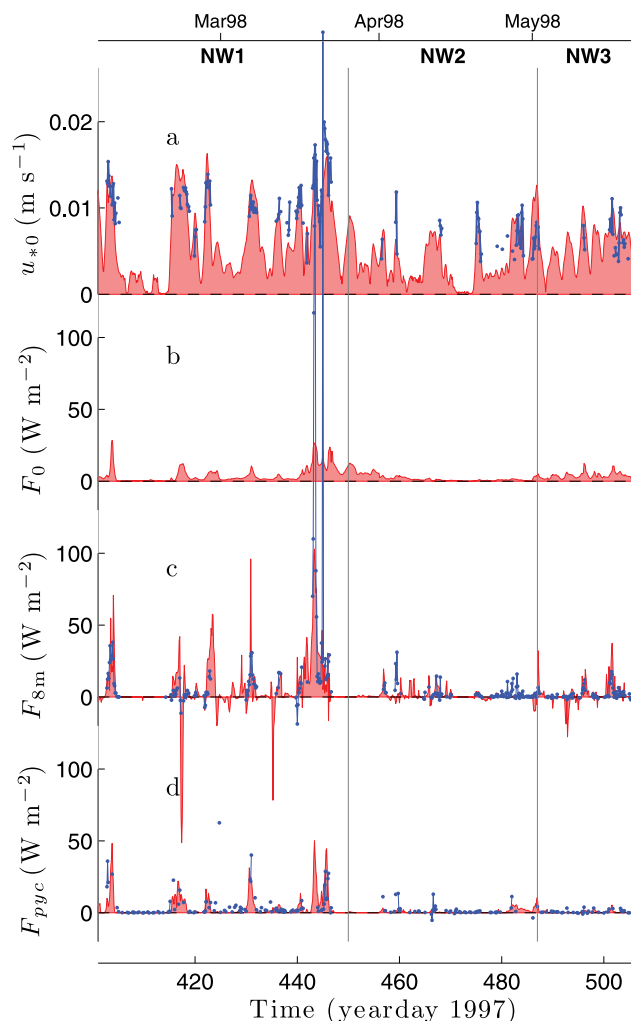


Figure 9. Same as Figure 8 but for segments NW1, NW2, and NW3.

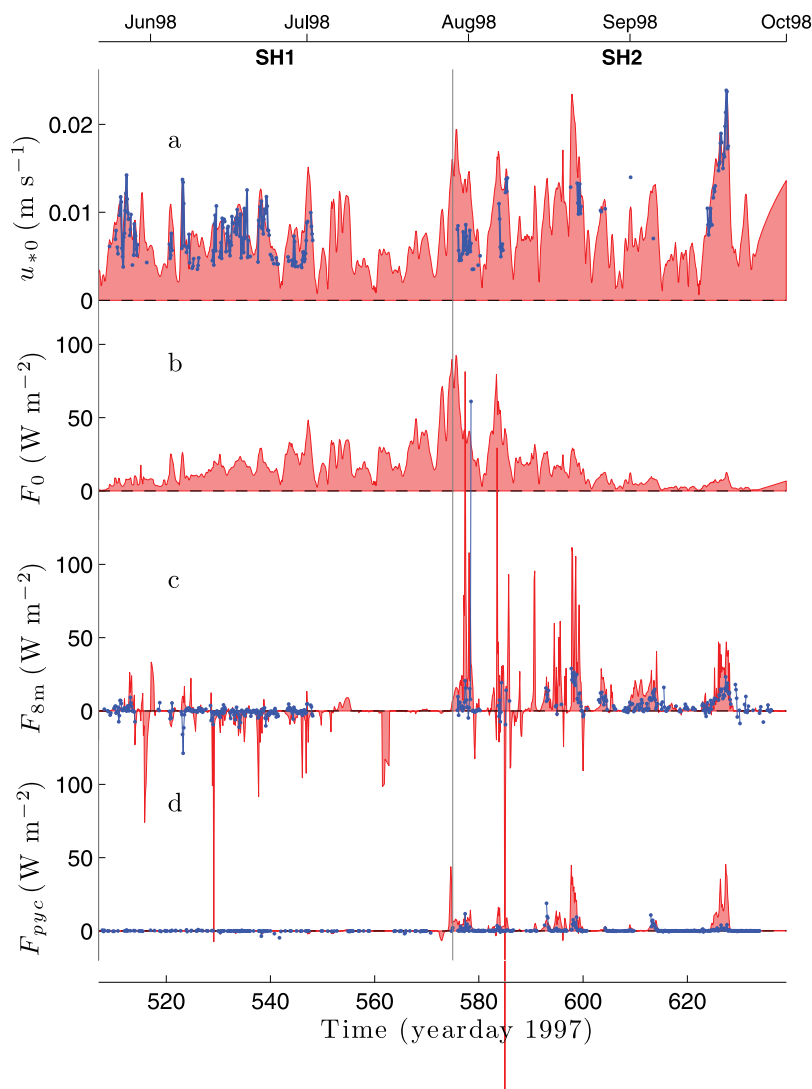


Figure 10. Same as Figure 8 but for segments SH1 and SH2.

emplaced in the upper pycnocline during the 1997 summer heating season.

4.2. Front

[40] Within the frontal segment FR (yearday 377–401), the ice camp drifted over strong horizontal gradients in the upper ocean as it approached the eastern flanks of the Northwind Ridge (Figure 5). The change consisted of an increase in salinity in the upper 100 m of the water column that was amplified near the surface. Surface salinity increased from 26.7 to 29.7 psu across the front; S_{pyc} also increased, but not as rapidly as S_{ml} , with the result that ΔS_{pyc} declined from 1.5 psu at the beginning of FR1 to 0.3 psu by the end of segment (Figure 6). Throughout most of the front T_{ml} remained near the freezing point. Although the heat content of the entrainment layer declined during FR (δT_{pyc} decreased from 0.79 K to 0.37 K, Figure 6), the heat content of the pycnocline below the entrainment layer increased (Figures 5d and 7c). The shallower temperature maxima found previously near 29 psu in the CB1 and CB2 segments diminished as the front was crossed and the salinity of the lower temperature maximum increased. By the end of FR, a single temperature

maximum existed at $S = 31.7$ psu, centered on about 57 m depth (30 m below the base of the mixed layer) and had a vertical extent of about 20 m. The temperature maximum was 1.03 C, the warmest temperature recorded during the experiment. This salinity front separates a Pacific-dominated pycnocline to the east from an Atlantic-dominated pycnocline to the west [see *McLaughlin et al.*, 2004, Figures 5 and 7]. $\delta^{18}O$ values in the front also indicate a large fraction of river input compared to the Deep Canada Basin [*Macdonald et al.*, 2002].

[41] With respect to the surface heat budget, FR1 is similar to the Canada Basin segments (i.e., F_0 was generally small even during storm-forced events with $u_{*0} > 0.01$ m s⁻¹), except for one event during which heat fluxes across the IOBL were quite large. Between day 390 and 394, ice speeds of up to 0.41 m s⁻¹ forced maximal u_{*0} of 0.025 m s⁻¹ (Figure 8a). The average of SLTC F_{pyc} during this event was 22.1 W m⁻². In contrast, the average microstructure F_{pyc} was only 2.7 W m⁻². The SLTC F_{8m} was 16.9 W m⁻² and the corresponding TIC heat flux was 10.5 W m⁻². Storm-averaged F_0 was 7.3 W m⁻². The microstructure estimates through the storm may be questionable, because this event

required the largest corrections to the spectral χ estimates (factor of 4–5 and greater, Figure 3). Heat flux values averaged over FR1 (Table 1) are dominated by this event. Even though there was a large amount of heat in the pycnocline, heat was entrained into the surface layer only during an unusually large storm that was able to overcome the strongly stratified upper pycnocline.

4.3. Northwind Ridge

[42] By the time the camp reached the eastern slope of the Northwind Ridge, the strong gradients of segment FR had diminished, and the upper ocean of segment NW1 (yearday 401–450) was characterized by the weakened stratification and increased upper pycnocline heat content that had developed as the front was crossed. Upper ocean statistics were more stationary during the Northwind/Chukchi Plateau segments than the three previous segments. NW1 segment-averaged δT_{pyc} was 0.83 K, the largest of the record (Table 1), and the average upper pycnocline stratification was $\Delta S_{pyc} = 0.3$ psu, significantly weaker than that observed during the Canada Basin or FR segments. The increase in δT_{pyc} was a reflection of a shoaling of the subsurface temperature maximum layer to within the entrainment layer (Figures 5d and 7d). This heat was contained in a temperature maximum of amplitude -0.63 C to 0.46 C, centered at salinity 31.7 psu, and occupying depth range 34 to 57 m. Segment-averaged T_{ml} showed a first departure from freezing (0.02 K) during NW1 but was elevated above freezing only during surface forcing events (Figure 6a), indicating the significance of entrainment processes to the heat content of the IOBL. Surface salinity continued to increase during this segment, from 30.0 to 30.8 psu.

[43] The camp crossed another front as it drifted from the Northwind Ridge Abyssal Plain onto the Chukchi Shelf that we chose as the boundary between segments NW1 and NW2. The subsurface temperature maximum was continuous across this front, but the amplitude of the maximum dropped significantly between NW1 and NW2 (Figures 7d and 7e). Although there was a large decrease in the heat content of the pycnocline as a whole (the temperature maximum was reduced to -0.97 C, on average), the decrease in temperature of the entrainment layer was more modest, δT_{pyc} decreased from 0.53 to 0.38 K, indicating that there was still a relatively large amount of heat just below the mixed layer. The heat content of the entrainment layer was steady because the decrease in amplitude of the subsurface temperature maximum was compensated to some extent by further shoaling of the depth of the temperature maximum layer. Surface salinity, surface temperature, and salinity gradient at the based of the mixed layer were similar to segment NW1.

[44] Beginning on yearday 486 (1 May 2008), δT_{ml} was sustained above zero (i.e., prior to this transition it was elevated only during strong forcing events), which is interpreted as the onset of radiation penetrating into the upper ocean. This transition was taken as the boundary between NW2 and NW3 (yeardays 486 to 507).

[45] The heat flux estimates of the Northwind portion of the drift before day 486 (NW1 and NW2) suggest a balance in which moderate ocean-to-ice heat fluxes are supported by entrainment of heat stored in the upper pycnocline (Figure 9). Segment-averaged microstructure F_{pyc} are 3.5–5.7 and 1.7–1.8 W m^{-2} for NW1 and NW2, respectively. SLTC values of

F_{pyc} averaged over those ensembles for which microstructure data were available are 5.5 and 0.6 W m^{-2} for NW1 and NW2, respectively. Averaged over all of the ensembles the SLTC values are 3.8 and 0.7 W m^{-2} . Average F_0 during NW1 and NW2 are 4.3 and 2.1 W m^{-2} . For NW1, then, a best estimate of F_{pyc} is close to 4 W m^{-2} , which is balanced by the average F_0 of 4.3 W m^{-2} , suggesting that essentially all of the entrained heat is ultimately transported to the ice. That the mixed layer heat budget was maintained primarily by a balance between F_{pyc} and F_0 is further evidenced by the fact that δT_{ml} deviated from zero only during the storm-forced events. During this period, storm-forced heat fluxes were coherent across the boundary layer (Figure 9). Large heat fluxes between days 442.5 and 446.5 were caused by a strong storm that forced localized upwelling *McPhee et al.* [2005]. The TICs provided measurements during this event but the CTD profiler was not operating because of the forced relocation of the profiler system described in section 2.1. Observed F_{8m} are much larger than SLTC F_{8m} because the SLTC is forced by interpolated CTD data that does not include the localized upwelling. CTD profiles before and after the event are similar suggesting that the SLTC results are representative of the ambient situation away from the localized upwelling.

[46] The SLTC- and microstructure-based F_{pyc} estimates are in better agreement during these weakly stratified conditions than in the earlier segments. Beyond day 486 (NW3), the surface heat fluxes were larger than the F_{pyc} estimates, consistent with the sustained departures from freezing noted above, most likely caused by insolation penetrating to the upper ocean. A combination of a reduced heat flux from below augmented by heat introduced by radiative forcing likely supported the continued NW3 average F_0 of 3.8 W m^{-2} .

4.4. Summer Heating

[47] The onset of basal ice melting on about day 507 (Figure 5b) is taken as the start of segment SH1. During SH1 (days 507–575), insolation substantially warmed the surface layer, as δT_{ml} increased from 0.01 to 0.30 K over the segment (Figure 6a). Near the beginning of SH1, coincidentally, the camp drifted northward off of the Chukchi shelf and through a hydrographic front. Across the front, S_{ml} increased rapidly from 30.7 to 31.9 psu and T_{pyc} decreased toward the freezing point; the average value of δT_{pyc} during SH1 was 0.16 K (the smallest segment-averaged value of the record). Increasing S_{ml} led to a reduction of water column stratification; the average and minimum values of ΔS_{pyc} were 0.2 and 0.02 psu (both the minimum of these statistics over the record). So, although the stratification was conducive to entrainment, there was very little heat contained in the entrainment layer to transport. *McLaughlin et al.* [2004] attribute the diminished heat content beyond the Chukchi Shelf to decreased fractions of Pacific origin water in the halocline, i.e., a transition to a “cold,” Atlantic halocline rather than a “cool,” Pacific halocline, using the terminology of *Steele et al.* [2004]. The almost complete lack of entrainment layer heat indicates that segment SH1 was clearly geographically separated from the spreading pathways of heat-containing Pacific Water. Thus, there is fairly complete separation of entrainment- and insolation-driven heat transport processes in the record.

[48] Following several weeks of quiescent conditions at the end of SH1 (Figure 10), a storm lasting from yearday 574 to 576 with peak u_{*0} of nearly 0.02 m s^{-1} mixed down a thin, fresh, and warm meltwater layer that had been trapped within leads and concavities on the ice underside [Skylvingstad *et al.*, 2003; Hayes and Morison, 2008]. This mixing event led to the development of the summer 1998 seasonal mixed layer and was taken as the beginning of the final segment SH2 (days 575–640). During the “mix-down,” S_{ml} decreased from 31.5 to 30.5 psu, h_{ml} shoaled from an average value of 33.2 during SH1 to a depth of 17 m (Figure 5), δS_{pyc} increased from about 0.1 to 0.5 psu, and heat was emplaced in the upper pycnocline, in a fashion similar to that seen at the beginning of the SHEBA record in segment CB1 and in the AIDJEX observations [Maykut and McPhee, 1995]. Entrainment layer heat content increased from δT_{pyc} of 0.1 to 0.25 K. Heat content of the surface layer reached its maximum just before the mix-down and decreased, more or less, over the period of SH2 until T_{ml} was at the freezing point by the end of the record. The heat content of the upper pycnocline remained steady, with δT_{pyc} about 0.25 K. A combination of surface forcing events and continued surface melting caused the surface layer to deepen and freshen for the remainder of SH2, as the camp moved northwestward off the Chukchi Plateau and over the deep water of the Mendeleyev Abyssal Plain.

[49] The insolation absorbed by the ocean surface layer during the summer heating season supported large ocean-to-ice heat fluxes (Figure 10b). The average values of F_0 during SH1 and SH 2 were 18.3 and 14.1 W m^{-2} , respectively. The lack of any significant heat in the entrainment layer during SH1 resulted in small segment-averaged F_{pyc} (0.1 W m^{-2} for both SLTC and microstructure). Model and observed heat fluxes within the mixed layer were negative during SH1, indicating that heat was transported downward from the thin, near-surface layer before the large mix-down occurred between SH1 and SH2. The segment average of TIC F_{8m} was -0.7 W m^{-2} and the average of SLTC F_{8m} was -3.2 W m^{-2} (-2.3 W m^{-2} for only those times with TIC estimates available). Most likely, the SLTC F_{8m} estimates are larger than the TIC estimates because of the near-surface stratification that was not captured by the profiling CTD data used to force the model. As a result of the heat emplaced in the upper pycnocline by the mix-down and subsequent mixed layer cooling, heat fluxes across the mixed layer base increased during SH2. The average value of the microstructure-based F_{pyc} was in the range 0.2 – 0.7 W m^{-2} and the average of SLTC F_{pyc} was 3.1 W m^{-2} (3.7 W m^{-2} for only those times for which microstructure estimates were available). Similar to CB1 and CB2, the SLTC estimates are significantly larger than the microstructure observations during this strongly stratified period. Average TIC F_{8m} were positive during CB2, but individual 3-h realizations had large positive and negative amplitudes (Figure 10c), highlighting the difficulty of representing the ocean-to-ice heat flux with eddy correlation measurements in the presence of incoming radiation. Because F_{pyc} was significantly smaller than F_0 during the summer, the ocean-to-ice flux must have been primarily supported by absorption of solar radiation within the mixed layer. During SH2, entrainment of heat emplaced in the upper pycnocline

was a minor heat source; using the segment-averaged SLTC value as an upper limit for F_{pyc} , not more than about 20% of F_0 could have possibly been supported by entrainment.

5. Surface Heat Budgets

[50] In order to quantify the significance of the ocean heat flux estimates described in the last section, we construct energy budgets for the ice cover by combining the SLTC interface heat flux, F_0 , with the results of the SHEBA ice and atmospheric boundary layer groups. Data from the ice group permits estimation of changes in internal energy of the ice cover, and the atmospheric boundary layer group provides estimates of the atmosphere-side surface energy flux, both of which can be compared to the magnitude of the ocean-to-ice heat flux. The sites of the ocean and atmospheric boundary layer measurements were chosen to be representative of undeformed, multiyear ice, while ice measurements were made in a variety of ice types. For the budget calculations we limit attention to data from two ice mass balance sites, “Pittsburgh” and “Quebec 2” (see Perovich *et al.* [2003] and additional description below), that were situated in undeformed, multiyear ice. The atmospheric flux tower, the hydroholes for the ocean observations, and the two ice sites were all within several hundred meters of each other. Two versions of the ice energy balance were attempted. A simple, ice base budget, similar to the one used by Perovich and Elder [2002], depends on only ocean and ice data and closes reasonably well. A second budget for the entire ice cover, which also requires the atmospheric fluxes, is not closed very well with the combined SHEBA observations.

5.1. Data and Calculations

[51] The atmospheric group has produced hourly estimates of all components of the surface atmospheric energy flux (i.e., atmosphere-to-ice energy flux, see Persson *et al.* [2002] for details; the data set is available at <http://www.eol.ucar.edu/projects/sheba/>),

$$F_a = Q_{short} + Q_{long} + H_s + H_l. \quad (7)$$

Here, Q_{short} is the net shortwave radiation, Q_{long} is the net longwave radiation, H_s is sensible heat flux, and H_l is latent heat flux. Positive fluxes are upward.

[52] The ice group measured changes in ice thickness on multiday time scales and obtained hourly profiles of ice temperature with thermistor strings embedded in the ice at sites representing different ice types (see Perovich *et al.* [2003] for details; the data set is available at <http://www.eol.ucar.edu/projects/sheba/>). Here, as described above, we use data from the Pittsburgh and Quebec 2. Both of these sites were instrumented with a single thermistor string through the ice and had three ice thickness gauges that provided data for the entire observational period.

[53] A budget for the change in internal energy of the whole ice cover may be written as

$$\frac{d}{dt}(E_s + E_i) = F_0 - F_a. \quad (8)$$

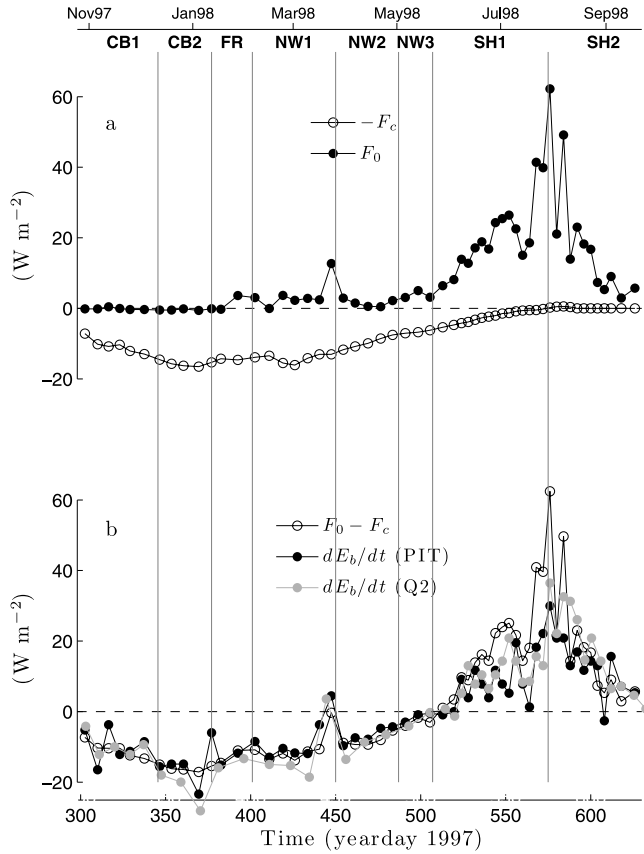


Figure 11. Time series of terms in the ice base energy budget (11): (a) comparison of the forcing ocean-to-ice F_0 and ice conductive F_c heat fluxes and (b) comparison of the net flux and tendency terms. In Figure 11b the tendency term is calculated for two ice mass balance sites: Pittsburgh and Quebec 2.

Here, the term on the left-hand side is the tendency of the ice internal energy, consisting of changes in sensible and latent heat, which is balanced by the divergence of energy flux between the ice base F_0 and the ice surface F_a . The time rate of change of latent heat in the ice cover was estimated as

$$\frac{dE_l}{dt} = \rho_0 L_f \left(\frac{dz_{bot}}{dt} - \frac{dz_{top}}{dt} \right), \quad (9)$$

where $L_f = 2.70 \times 10^5 \text{ J kg}^{-1}$ is the latent heat of fusion for sea ice with salinity of 6 psu, and $\frac{dz_{bot}}{dt}$ and $\frac{dz_{top}}{dt}$ are the rates of change of the vertical positions of bottom and top surfaces of the ice, respectively. The time rate of change of the sensible heat of the ice cover was estimated as

$$\frac{dE_s}{dt} = \rho_{ice} c_p \frac{d}{dt} \int_{z_{bot}}^{z_{top}} T_{ice} dz, \quad (10)$$

where $\rho_{ice} = 900 \text{ kg m}^{-3}$ is density of sea ice, c_p is specific heat of sea ice, the Pittsburgh site thermistor string provided the ice temperature T_{ice} , and the limits of integration were determined by interpolation of the ice thickness measurements made at the Pittsburgh site. The calculations do

not take account of the energy required to melt snow, but *Perovich et al.* [2003] estimate that this energy was less than 20% of that required to produce the observed surface ice melt.

[54] The ice base energy budget applies to a thin layer at the base of the ice cover,

$$\frac{dE_b}{dt} = F_0 - F_c \quad (11)$$

Here, $\frac{dE_b}{dt}$ is the rate of change of latent heat associated with ice growth and bottom melt, given by the first term on the right-hand side of (9). The latent heat term is calculated separately from Pittsburgh and Quebec 2 thickness measurements in order to provide a check on the representativeness of these measurements. The conductive heat flux at the base of the ice F_c was estimated using

$$F_c = k_{ice} \left. \frac{\partial T}{\partial z} \right|_b, \quad (12)$$

where $k_{ice} = 2.0 \text{ W m K}^{-1}$ [*Sturm et al.*, 2002] is the conductivity of sea ice and $\left. \frac{\partial T}{\partial z} \right|_b$ is the temperature gradient near the base of the ice, estimated from the Pittsburgh thermistor data by tracking the location of the bottom of the ice. This budget has the advantages of being more directly impacted by the ocean flux and simpler than the whole ice thickness budget.

[55] Because the ice thickness measurements had the lowest temporal resolution of all the measurements contributing to (8) and (11), the terms in the two budgets were calculated over periods delimited by the times of the ice thickness measurements. The latent heat tendency terms were then calculated using first differences across each period and the other terms were calculated as averages over each period. The resulting estimates had temporal resolutions of about a week during ice growth and about 4 days during the melting season, when the ice thickness measurements were made more frequently. Segment-averaged values of the ice base budget quantities $F_0 - F_c$ and dE_b/dt are listed in Table 1.

5.2. Results

[56] With one exception, the ice base energy budget (11) is closed remarkably well by the SHEBA ocean and ice observations (Figure 11b). During the Canada Basin segments, F_0 is relatively small, and basal ice growth is determined completely by the conductive flux at the base of the ice. During the Front and Northwind segments, however, the ocean heat flux makes a meaningful contribution to the budget (Figure 11a). For example, averaged over segment NW1, F_0 is 30% of $F_c = 14.2 \text{ W m}^{-2}$ (Table 1) and, over NW2, F_0 is 10% of $F_c = 9.8 \text{ W m}^{-2}$. In terms of its impact on the annual surface heat budget, wintertime ocean-to-ice heat fluxes above the Chukchi Borderland reduced ice growth on the SHEBA floe by about 15% compared to the case of near-zero wintertime F_0 . During segments FR, NW1, NW2, and to a lesser extent NW3, the averaged F_{pyc} and F_0 estimates are nearly equal (Table 1), demonstrating that the ocean-to-ice heat flux was supported largely by the entrainment of heat stored in the upper pycnocline over this period. *Perovich and Elder* [2002] and *Perovich et al.* [2003] note that around

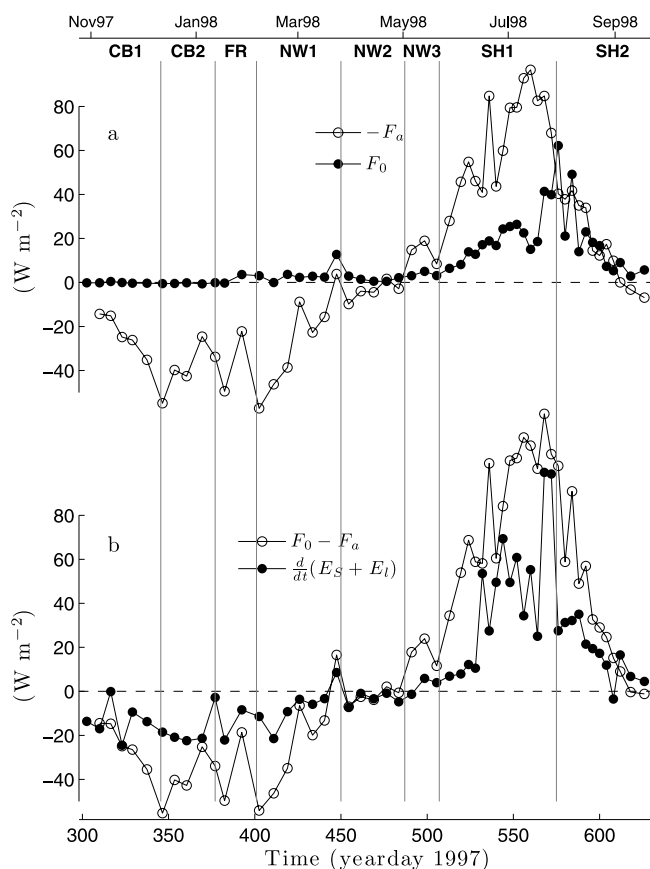


Figure 12. Time series of terms in the ice cover energy budget (8): (a) comparison of the forcing ocean-to-ice F_0 and ice-to-atmosphere F_a energy fluxes and (b) comparison of the net flux and tendency terms.

day 448, the base of the ice melted during the ocean upwelling event that was described by *McPhee et al.* [2005]. This event is reflected in the ice base budget. On day 448, F_0 exceeded the conductive flux, and this convergence of heat transport resulted in basal melting; that is, dE_b/dt was greater than zero. The SLTC-based F_0 estimate is not large enough to completely explain the observed melt rates during this event. But, as described in section 2.1, the CTD was not in operation during this period, so the SLTC heat flux results are based on interpolated T and S profiles that do not include the upwelling reported by *McPhee et al.* [2005] and are therefore biased low. Significantly, during segments NW1 and NW2, the ocean fluxes are required to close the ice base budget. Good agreement between the Pittsburgh and Quebec 2 site thickness estimates and the closure of the ice base budget indicates that the ocean and ice measurements have successfully characterized basal melt and growth of multiyear ice during wintertime at the field site.

[57] During the summer heating season, the ice base budget does not close as well as it does during winter (Figure 11 and Table 1). At the start of SH1, F_c and F_0 had similar amplitudes, but by the end of SH1, the ice cover was approximately isothermal at the melting point and the conductive flux had gone to zero (Figure 11). This condition prevails throughout SH2, and the ice cover budget is

maintained by F_0 melting the bottom of the ice. For the latter half of SH1, F_0 was significantly larger than dE_b/dt for both the Pittsburgh and Quebec 2 sites. Average SH1 values of $F_0 - F_c$ and dE_b/dt are 15.7 and 8.6 W m^{-2} , respectively. In contrast, the ice base budget closes reasonably well for SH2, after the mix-down of the thin surface layer around yearday 575, during which average values of $F_0 - F_c$ and dE_b/dt are 14.2 and 14.0 W m^{-2} , respectively. Over the summer heating season, F_0 , $F_0 - F_c$, and dE_b/dt had average values of 16.3 , 14.9 , and 11.1 W m^{-2} , or an almost 4 W m^{-2} imbalance in the basal energy budget (Table 1).

[58] The energy budget for the whole of the ice cover (8) does not close very well (Figure 12). The combined ice thickness and temperature data show that the ice cover lost energy from the start of the record to approximately day 500 (214 days total, before the onset of melting) at an average rate of 7 W m^{-2} . In principle, the winter energy loss should have been balanced by the difference between the atmospheric energy flux and the surface oceanic heat flux, but the average atmospheric flux was 21 W m^{-2} while the average ocean surface heat flux was 1 W m^{-2} . The magnitude of the net atmospheric flux also appears to be too large during the melting season, the fluxes indicate that more heat entered the ice than can be explained by the change in ice internal energy. The amplitude of the net flux, $F_0 - F_a$, is greater than the estimated changes in ice cover energy during both ice growth and melting by a factor of 2.0 based on linear regression.

6. Discussion

[59] The heat flux estimates indicate that the dominant source of heat for melting the bottom of the ice during SHEBA was incoming solar radiation absorbed by the upper ocean, with upward transport from heat-carrying, Pacific origin water playing a secondary role. The question of how much of the Pacific origin, upper halocline heat was actually transported through the Bering Strait, in comparison to the amount emplaced by summer insolation over the Chukchi Shelf remains unresolved. But the results do indicate that the remote advection of heat to the Chukchi Borderlands affected the ice cover energy budget. Over the SHEBA year, the average ocean-to-ice heat flux was 7.6 W m^{-2} and the average pycnocline heat flux was 1.8 W m^{-2} from the SLTC model and 1.2 W m^{-2} from the thermal microstructure data (Table 1). So, the measurements and model indicate that about 16–24% of the ocean-to-ice heat flux was supplied by entrainment of heat from below the mixed layer. The most likely source for the remainder was solar input. Along the SHEBA drift, the entrainment fluxes were large during winter while the station was in the vicinity of the Northwind Ridge (Figure 9), and this resulted in a modest reduction in ice growth (Figure 11). Temperature data from a mooring on the Northwind Ridge during the same time period as the SHEBA drift [*Shimada et al.*, 2001] show that the upper pycnocline in the area contained large amounts of heat from about yeardays 350–575, suggesting that, above the Northwind Ridge, the impact of the entrainment fluxes was larger than estimated from the SHEBA drift, which was located in this region from about yeardays 400–507. For example, model and data indicate that the entrainment heat flux was about 4 – 5 W m^{-2}

directly above the Northwind Ridge and abyssal Plain (segment FR1, Table 1), which corresponds to a 28–35% decrease in ice growth from the condition of near-zero ocean-to-ice heat flux. It thus seems plausible that the vertical transport of heat from shallow Pacific origin layer did play a role in preconditioning the upper ocean and ice cover in the vicinity of the Northwind Ridge for the large 1998 summer melt observed in the area, as suggested by Shimada *et al.* [2001].

[60] One of the largest surprises amongst the SHEBA observations was the large amount of bottom melting during the 1998 summer [see Perovich *et al.*, 2003]. The heat flux estimates from this period show that the role of the upper ocean during this period was primarily that of a reservoir for storing and locally distributing incoming radiation. During the summer period, there was very little heat contained in the upper pycnocline, because by about yearday 507 (29 July 1998) the ice camp had passed off of the Chukchi Shelf, away from the influence of Pacific origin water. As a result summertime entrainment heat fluxes were about 1 W m^{-2} and were not significant in terms of the surface heat budget. By accounting for solar energy input through open water and different ice types and thicknesses (including the thin, undeformed, multiyear ice observed at the SHEBA site), Perovich [2005] has accounted for the energy required to support the observed ocean-to-ice heat fluxes and bottom melt rates.

[61] Overall, the SHEBA ice and upper ocean observations close the ice base energy budget reasonably well, with the exception of the beginning of the melt season (segment SH1, Figure 11). During SH1, the average ocean-to-ice heat flux estimate of 18.3 W m^{-2} led to a heat flux divergence at the bottom of the ice $F_0 - F_c = 15.7 \text{ W m}^{-2}$, that was about twice as large as the observed rate of change of latent heat of 8.6 W m^{-2} . The presence of a thin (order 1 m), fresh, and warm, near-surface layer [see Skillingstad *et al.*, 2003, Figure 1], which was not resolved by profiling CTD, is a likely candidate for affecting the ocean-to-ice heat flux estimates, but the actual mechanisms involved are not clear. Interestingly the ice base energy budget closes well during segment SH2, after the “mix-down.”

[62] To provide historical and spatial context, temperature and salinity from deep SHEBA CTD casts are plotted as anomalies from the 1950–1987 average winter climatology [Arctic Climatology Project, 1998] in Figure 13. Overall, the upper ocean along the SHEBA drift was saltier and slightly warmer than climatology. Because the yearlong drift of SHEBA is being compared to the winter climatology, this comparison is conservative with respect to seasonal variation for most parts of the drift. The exception is the fresh surface anomaly and warm temperature anomaly at 50 m in the Beaufort Sea at the beginning of the SHEBA drift (i.e., CB1 in Figure 5). Here we are comparing early fall SHEBA observations to winter climatology and so might expect fresh and warm anomalies, but the freshening of the mixed layer at the beginning of the drift relative to previous summers is well established [McPhee *et al.*, 1998; Macdonald *et al.*, 1999].

[63] Aside from CB1, positive temperature anomalies occurred either during winter in association with the subsurface temperature maximum layer described in section 4.3

or at depth in the lower pycnocline. The largest positive temperature anomalies (2°C) occurred in the subsurface temperature maximum layers over the Northwind Ridge and Chukchi Shelf and in the Atlantic Water layer at 200–300 m in the Chukchi borderland region. The latter was associated with the easternmost extension of Atlantic water warming in the early 1990s [Carmack *et al.*, 1995; Morison *et al.*, 1998] and described by McLaughlin *et al.* [2004] for SHEBA.

[64] Except for CB1 and the very surface at the end of the SHEBA drift (SH2), the upper ocean water column was saltier than climatology by 0.5 to 2 psu, with larger anomalies associated with the Pacific-Atlantic front. Near the surface, the mixed layer was 2 psu saltier than climatology over the Chukchi Shelf and Plateau. Similar to the SHEBA-observed Atlantic Water temperature anomalies, the increased upper ocean salinity is consistent with the cyclonic shift of the Pacific-Atlantic front that began in the early 1990s [Carmack *et al.*, 1995; Morison *et al.*, 1998]. These upper ocean salinity anomalies, related to basin-wide changes, accounted for a large portion of the observed variability in the stratification across the upper pycnocline (ΔS_{pyc} , Figure 6), and thus played a significant role in regulating the amount of heat transport into the surface layer from heat-containing waters below.

[65] The comparison of SLTC model and thermal microstructure-based estimates of the heat flux entering the surface layer from the upper pycnocline (F_{pyc} , Figures 8–10 and Table 1) showed that the model fluxes were larger than the observational estimates during the strongly stratified periods at the beginning and end of the drift and that the model and observations were in reasonable agreement during the more weakly stratified period over the Chukchi Borderlands topography. A possible explanation is that the Richardson number dependence of the ratio of scalar eddy diffusivity to eddy viscosity in the model is too weak under highly stratified conditions. In addition to stratification effects, though, Pinkel [2005] has documented an increase in upward propagating internal wave energy in the regions of steep topography along the SHEBA drift. So it is also possible that the comparison between observed and modeled fluxes is affected by internal-wave-driven mixing processes, which are not explicitly included in the SLTC model.

[66] A failure of the SHEBA observations is the inability to close the energy budget for the entire ice cover, including, ocean and atmospheric energy fluxes (Figure 12). As pointed out in the introduction, [Persson *et al.*, 2002] find that the annual average of the net atmospheric energy flux is balanced by the annual-averaged conductive flux and total surface melt, but the budget does not close well seasonally. The wintertime net atmospheric flux during implies more ice growth than observed and the summertime net atmospheric flux implies more surface melt than observed. The relatively good closure of the ice base budget indicates that the ocean flux and ice thickness measurements are fairly accurate and representative, which suggests that the problem with the whole ice cover budget lies with the net atmospheric flux. A second possibility is that, although bottom ablation estimates appear to be representative, the surface ablation estimates may not be. The difficulty in

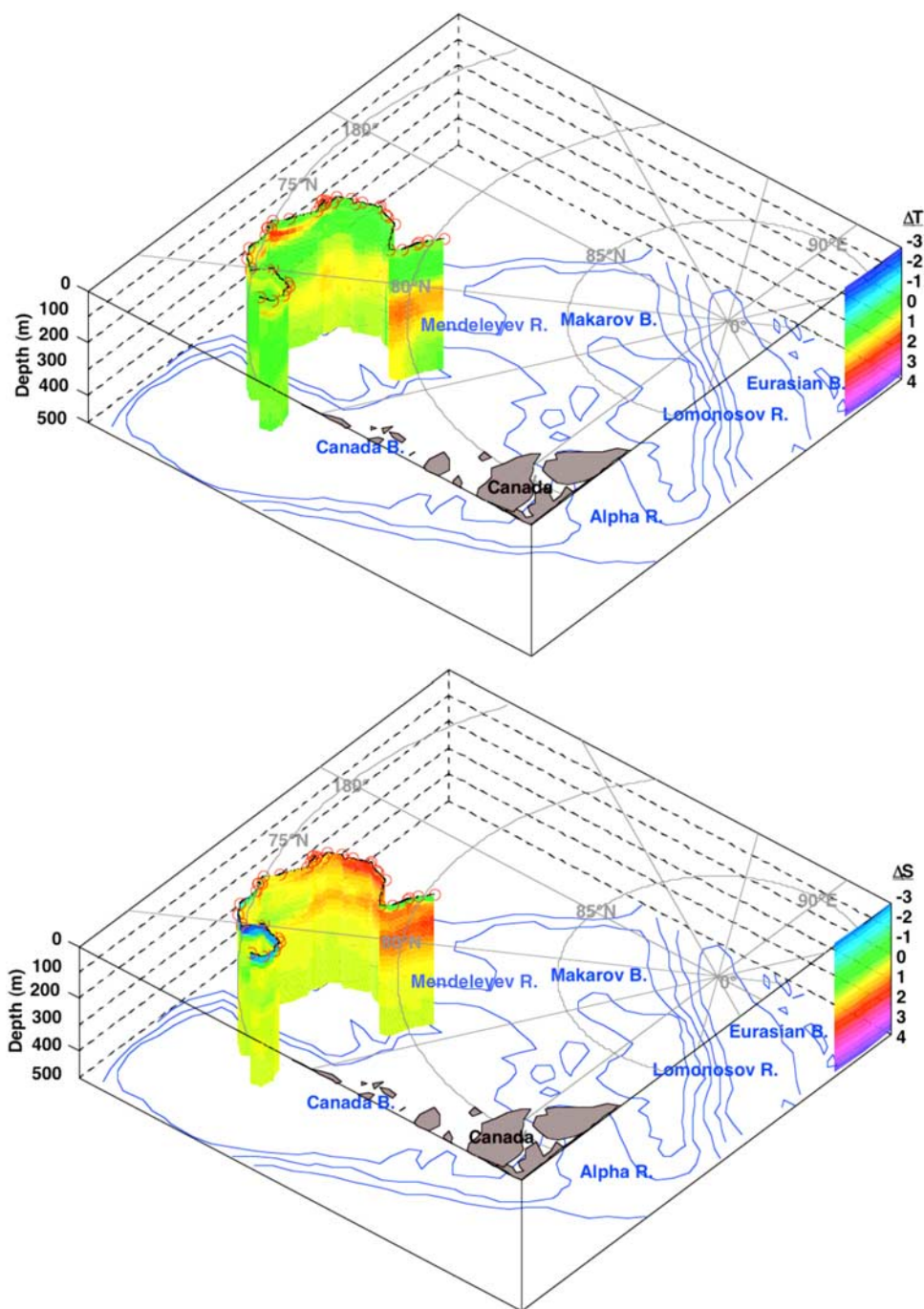


Figure 13. Sections of SHEBA (top) temperature and (bottom) salinity anomalies relative to the EWG Gridded Climatology 1950–1987.

closing the air-ice side of the budget is not surprising as the air-ice energy balance is more complicated than the ice-water balance, and the evolution of the topside of the ice is more complex (e.g., melting of snow and formation of melt ponds) than that of the underside of the ice. Although the overall budget does not close seasonally, the annual averages of the ocean-to-ice heat flux and the excess atmospheric flux do agree well with observed ice melt. The annual average of ocean-to-ice heat flux (7.6 W m^{-2}) is close to the annual average of the atmospheric flux excess (8.2 W m^{-2} [Persson *et al.*, 2002]), which demonstrates

that ocean and atmosphere played equal roles in melting the ice during the SHEBA year.

7. Summary and Conclusions

[67] The upper ocean below the SHEBA ice camp experienced substantial seasonal and geographic variability in temperature and salinity, which directly impacted the oceanic heat flux profile. During the initial part of the record, as the camp drifted over the Canada Basin, the upper pycnocline contained moderate amounts of heat, but strong

stratification effectively insulated this heat from mixed layer turbulence: heat fluxes at the base of the mixed layer and at the ocean-ice interface were small ($0.2\text{--}1.2$ and 0.2 W m^{-2} , respectively). During the middle portion of the record, as the camp drifted over the Northwind Ridge and the Chukchi Shelf, the presence of relatively warm and salty Pacific origin water led to a dramatic increase in upper pycnocline heat content and a reduction in upper pycnocline stratification, which permitted moderate pycnocline heat fluxes ($2.1\text{--}3.7\text{ W m}^{-2}$) and moderate ocean-to-ice heat fluxes (3.5 W m^{-2}). As expected, solar insolation was the dominant heat source during the final, summertime portion of the drift. During the heating period, the pycnocline heat flux was relatively small ($0.1\text{--}1.5\text{ W m}^{-2}$) while the interface heat flux was large (16.3 W m^{-2}). The average value of ocean-to-ice heat flux over the entire record was 7.6 W m^{-2} .

[68] Energy budgets for the ice cover were constructed to investigate the significance of the ocean-to-ice heat fluxes with respect to the mass balance of sea ice. The oceanic contribution to the budget during the middle portion of the drift, which was supported by entrainment of heat stored in the upper pycnocline, was responsible for a modest reduction in ice growth during the winter season (15%). During the summer heating season, the ocean-to-ice heat flux estimates are somewhat larger than the latent energy changes associated with basal melting.

[69] **Acknowledgments.** Jim Stockel contributed significantly to the acquisition and processing of the CTD and thermal microstructure data. The careful reading of the manuscript by two anonymous reviewers led to significant improvements. This work was supported by the National Science Foundation Office of Polar Programs through awards OPP-9701391 and OPP-0084296.

References

- Aagaard, K., L. K. Coachman, and E. C. Carmack (1981), On the halocline of the Arctic Ocean, *Deep Sea Res., Part A*, 28(6), 529–545.
- Arctic Climatology Project (1998), *Environmental Working Group Joint U.S.-Russian Atlas of the Arctic Ocean—Summer Period* [CD-ROM], edited by L. Timokhov and F. Tanis, Environ. Res. Inst. of Mich., Ann Arbor.
- Boyd, T. J., M. Steele, R. D. Muench, and J. T. Gunn (2002), Partial recovery of the Arctic Ocean halocline, *Geophys. Res. Lett.*, 29(14), 1657, doi:10.1029/2001GL014047.
- Carmack, E. C., R. W. Macdonald, R. Perkin, F. A. McLaughlin, and R. J. Pearson (1995), Evidence for warming of Atlantic water in the southern Canadian Basin of the Arctic Ocean: Results from the Larsen-93 Expedition, *Geophys. Res. Lett.*, 22, 1061–1064.
- Curry, J. A., J. L. Schramm, and E. E. Ebert (1995), Sea-ice albedo climate feedback mechanism, *J. Clim.*, 8, 240–247.
- D'Asaro, E. A., and J. H. Morison (1992), Internal waves and mixing in the Arctic Ocean, *Deep Sea Res., Part A*, 39, S459–S484.
- Fleury, M., and R. G. Lueck (1994), Direct heat-flux estimates using a towed vehicle, *J. Phys. Oceanogr.*, 24, 801–818.
- Gregg, M. C. (1999), Uncertainties and limitations in measuring epsilon and chi(tau), *J. Atmos. Oceanic Technol.*, 16, 1483–1490.
- Gunn, J. T., and R. D. Muench (2001), Observed changes in Arctic Ocean temperature structure over the past half decade, *Geophys. Res. Lett.*, 28, 1035–1038.
- Hayes, D. R. (2003), The heat and salt balances of the upper ocean beneath a spatially variable melting sea ice cover, Ph.D. thesis, Univ. of Wash., Seattle.
- Hayes, D. R., and J. H. Morison (2008), Ice-ocean turbulent exchange in the arctic summer measured by an autonomous underwater vehicle, *Limnol. Oceanogr.*, 53, 2287–2308.
- Kadko, D. (2000), Modeling the evolution of the Arctic mixed layer during the fall 1997 Surface Heat Budget of the Arctic Ocean (SHEBA) Project using measurements of Be-7, *J. Geophys. Res.*, 105, 3369–3378.
- Kadko, D., and P. Swart (2004), The source of the high heat and freshwater content of the upper ocean at the SHEBA site in the Beaufort Sea in 1997, *J. Geophys. Res.*, 109, C01022, doi:10.1029/2002JC001734.
- Kellog, W. W. (1973), Climate feedback mechanisms involving the polar regions, in *Climate of the Arctic*, edited by G. Weller and S. A. Bowling, pp. 111–116, Geophys. Inst., Fairbanks, Alaska.
- Macdonald, R. W., E. C. Carmack, F. A. McLaughlin, K. K. Falkner, and J. H. Swift (1999), Connections among ice, runoff and atmospheric forcing in the Beaufort Gyre, *Geophys. Res. Lett.*, 26(15), 2223–2226.
- Macdonald, R. W., F. A. McLaughlin, and E. C. Carmack (2002), Fresh water and its sources during the SHEBA drift in the Canada Basin of the Arctic Ocean, *Deep Sea Res., Part 1*, 49(10), 1769–1785.
- Maykut, G. A. (1982), Large-scale heat-exchange and ice production in the central Arctic, *J. Geophys. Res.*, 87, 7971–7984.
- Maykut, G. A., and M. G. McPhee (1995), Solar heating of the Arctic mixed layer, *J. Geophys. Res.*, 100(C12), 24,691–24,703.
- Maykut, G. A., and N. Untersteiner (1971), Some results from a time-dependent thermodynamic model of sea ice, *J. Geophys. Res.*, 76(6), 1550–1575.
- McLaughlin, F. A., E. C. Carmack, R. W. Macdonald, H. Melling, J. H. Swift, P. A. Wheeler, B. F. Sherr, and E. B. Sherr (2004), The joint roles of Pacific and Atlantic-origin waters in the Canada Basin, 1997–1998, *Deep Sea Res., Part 1*, 51, 107–128.
- McPhee, M. G. (1981), An analytic similarity theory for the planetary boundary layer stabilized by surface buoyancy, *Boundary Layer Meteorol.*, 21(3), 325–339.
- McPhee, M. G. (1999), Parameterization of mixing in the ocean boundary layer, *J. Mar. Syst.*, 21(1–4), 55–65.
- McPhee, M. G. (2002), Turbulent stress at the ice/ocean interface and bottom surface hydraulic roughness during the sheba drift, *J. Geophys. Res.*, 107(C10), 8037, doi:10.1029/2000JC000633.
- McPhee, M. G. (2008), *Air-Ice-Ocean Interaction: Turbulent Ocean Boundary Layer Exchange Processes*, Springer, New York.
- McPhee, M. G., T. P. Stanton, J. H. Morison, and D. G. Martinson (1998), Freshening of the upper ocean in the Arctic: Is perennial sea ice disappearing?, *Geophys. Res. Lett.*, 25(10), 1729–1732.
- McPhee, M. G., T. Kikuchi, J. H. Morison, and T. P. Stanton (2003), Ocean-to-ice heat flux at the North Pole environmental observatory, *Geophys. Res. Lett.*, 30(24), 2274, doi:10.1029/2003GL018580.
- McPhee, M. G., R. Kwok, R. Robins, and M. Coon (2005), Upwelling of Arctic pycnocline associated with shear motion of sea ice, *Geophys. Res. Lett.*, 32, L10616, doi:10.1029/2004GL021819.
- McPhee, M. G., J. H. Morison, and F. Nilsen (2008), Revisiting heat and salt exchange at the ice-ocean interface: Ocean flux and modeling considerations, *J. Geophys. Res.*, 113, C06014, doi:10.1029/2007JC004383.
- Morison, J., M. Steele, and R. Andersen (1998), Hydrography of the upper Arctic Ocean measured from the nuclear submarine USS Pargo, *Deep Sea Res., Part 1*, 45(1), 15–38.
- Morison, J., M. Steele, T. Kikuchi, K. Falkner, and W. Smethie (2006), Relaxation of central Arctic Ocean hydrography to pre-1990s climatology, *Geophys. Res. Lett.*, 33, L17604, doi:10.1029/2006GL026826.
- Morison, J., J. Wahr, R. Kwok, and C. Peralta-Ferriz (2007), Recent trends in Arctic Ocean mass distribution revealed by GRACE, *Geophys. Res. Lett.*, 34, L07602, doi:10.1029/2006GL029016.
- Mudge, T. D., and R. G. Lueck (1994), Digital signal-processing to enhance oceanographic observations, *J. Atmos. Oceanic Technol.*, 11, 825–836.
- Osborn, T. R. (1980), Estimates of the local-rate of vertical diffusion from dissipation measurements, *J. Phys. Oceanogr.*, 10(1), 83–89.
- Osborn, T. R., and C. S. Cox (1972), Oceanic fine structure, *Geophys. Fluid Dyn.*, 3, 321–345.
- Perovich, D. K. (2005), On the aggregate-scale partitioning of solar radiation in Arctic sea ice during the Surface Heat Budget of the Arctic Ocean (SHEBA) field experiment, *J. Geophys. Res.*, 110, C03002, doi:10.1029/2004JC002512.
- Perovich, D. K., and B. Elder (2002), Estimates of ocean heat flux at SHEBA, *Geophys. Res. Lett.*, 29(9), 1344, doi:10.1029/2001GL014171.
- Perovich, D. K., and R. E. Moritz (2002), Preface, *J. Geophys. Res.*, 107(C10), 8026, doi:10.1029/2002JC001314.
- Perovich, D. K., T. C. Grenfell, J. A. Richter-Menge, B. Light, W. B. Tucker, and H. Eicken (2003), Thin and thinner: Sea ice mass balance measurements during SHEBA, *J. Geophys. Res.*, 108(C3), 8050, doi:10.1029/2001JC001079.
- Persson, P. O. G., C. W. Fairall, E. L. Andreas, P. S. Guest, and D. K. Perovich (2002), Measurements near the Atmospheric Surface Flux Group tower at SHEBA: Near-surface conditions and surface energy budget, *J. Geophys. Res.*, 107(C10), 8045, doi:10.1029/2000JC000705.
- Pinkel, R. (2005), Near-inertial wave propagation in the western Arctic, *J. Phys. Oceanogr.*, 35, 645–665.
- Shaw, W. J., J. H. Trowbridge, and A. J. Williams (2001), Budgets of turbulent kinetic energy and scalar variance in the continental shelf bottom boundary layer, *J. Geophys. Res.*, 106, 9551–9564.
- Shimada, K., E. C. Carmack, K. Hatakeyama, and T. Takizawa (2001), Varieties of shallow temperature maximum waters in the Western

- Canadian Basin of the Arctic Ocean, *Geophys. Res. Lett.*, 28(18), 3441–3444.
- Skyllingstad, E. D., C. A. Paulson, W. S. Pegau, M. G. McPhee, and T. Stanton (2003), Effects of keels on ice bottom turbulence exchange, *J. Geophys. Res.*, 108(C12), 3372, doi:10.1029/2002JC001488.
- Skyllingstad, E. D., C. A. Paulson, and W. S. Pegau (2005), Simulation of turbulent exchange processes in summertime leads, *J. Geophys. Res.*, 110, C05021, doi:10.1029/2004JC002502.
- Steele, M., and T. Boyd (1998), Retreat of the cold halocline layer in the Arctic Ocean, *J. Geophys. Res.*, 103(C5), 10,419–10,435.
- Steele, M., J. Morison, W. Ermold, I. Rigor, M. Ortmeyer, and K. Shimada (2004), Circulation of summer Pacific halocline water in the Arctic Ocean, *J. Geophys. Res.*, 109, C02027, doi:10.1029/2003JC002009.
- Sturm, M., D. K. Perovich, and J. Holmgren (2002), Thermal conductivity and heat transfer through the snow on the ice of the Beaufort Sea, *J. Geophys. Res.*, 107(C21), 8043, doi:10.1029/2000JC000409.
- Uttal, T., et al. (2002), Surface heat budget of the Arctic Ocean, *Bull. Am. Meteorol. Soc.*, 83(2), 255–275.
- Walsh, D., I. Polyakov, L. Timokhov, and E. Carmack (2007), Thermohaline structure and variability in the eastern Nansen Basin as seen from historical data, *J. Mar. Res.*, 65(5), 685–714.
- Woodgate, R. A., K. Aagaard, and T. J. Weingartner (2005), Monthly temperature, salinity, and transport variability of the Bering Strait through flow, *Geophys. Res. Lett.*, 32, L04601, doi:10.1029/2004GL021880.
-
- D. G. Martinson, Lamont-Doherty Earth Observatory, Earth Institute at Columbia University, Palisades, NY 10964, USA.
- M. G. McPhee, McPhee Research Company, Naches, WA 98937, USA.
- J. H. Morison, Polar Science Center, Applied Physics Laboratory, University of Washington, Seattle, WA 98105, USA.
- W. J. Shaw and T. P. Stanton, Oceanography Department, Naval Postgraduate School, Monterey, CA 93943, USA. (wjshaw@nps.edu)